Disease Models & Mechanisms 6, 342-357 (2013) doi:10.1242/dmm.010140

Exacerbated neuronal ceroid lipofuscinosis phenotype in *Cln1/5* double-knockout mice

Tea Blom[1,2], Mia-Lisa Schmiedt[1,2], Andrew M. Wong[3], Aija Kyttälä[1,2], Jarkko Soronen[1,2], Matti Jauhiainen[1], Jaana Tyynelä[4], Jonathan D. Cooper[3] and Anu Jalanko[1,2,*]

SUMMARY

Both *CLN1* and *CLN5* deficiencies lead to severe neurodegenerative diseases of childhood, known as neuronal ceroid lipofuscinoses (NCLs). The broadly similar phenotypes of NCL mouse models, and the potential for interactions between NCL proteins, raise the possibility of shared or convergent disease mechanisms. To begin addressing these issues, we have developed a new mouse model lacking both *Cln1* and *Cln5* genes. These double-knockout (*Cln1/5* dko) mice were fertile, showing a slight decrease in expected Mendelian breeding ratios, as well as impaired embryoid body formation by induced pluripotent stem cells derived from *Cln1/5* dko fibroblasts. Typical disease manifestations of the NCLs, i.e. seizures and motor dysfunction, were detected at the age of 3 months, earlier than in either single knockout mouse. Pathological analyses revealed a similar exacerbation and earlier onset of disease in *Cln1/5* dko mice, which exhibited a pronounced accumulation of autofluorescent storage material. Cortical demyelination and more pronounced glial activation in cortical and thalamic regions was followed by cortical neuron loss. Alterations in lipid metabolism in *Cln1/5* dko showed a specific increase in plasma phospholipid transfer protein (PLTP) activity. Finally, gene expression profiling of *Cln1/5* dko cortex revealed defects in myelination and immune response pathways, with a prominent downregulation of α-synuclein in *Cln1/5* dko mouse brains. The simultaneous loss of both *Cln1* and *Cln5* genes might enhance the typical pathological phenotypes of these mice by disrupting or downregulating shared or convergent pathogenic pathways, which could potentially include interactions of CLN1 and CLN5.

INTRODUCTION

The neuronal ceroid lipofuscinoses (NCLs) represent the most frequent group of inherited neurodegenerative diseases in children, with an estimated worldwide incidence of 1:14,000 to 1:67,000, depending on ethnic group and the founder group effect (Santavuori, 1988; Haltia, 2006; Mole et al., 2011). The NCLs are characterized by progressive visual and mental decline, motor disturbances, epilepsy and behavioral changes, ultimately leading to premature death. These autosomal recessive diseases are caused by mutations in at least ten genes, including eight conventional NCL-associated genes (*CLN1*, *CLN2*, *CLN3*, *CLN5*, *CLN6*, *CLN7*/*MFSD8*, *CLN8* and *CTSD*/*CLN10*), and two additional genes (*DNAJC5* and *SGSH*) (Kousi et al., 2012). Despite this genetic heterogeneity, the NCLs display a relatively uniform phenotype in the central nervous system (CNS), characterized by a dramatic loss of cortical neurons, and accumulation of lysosomal autofluorescent lipopigments (Jalanko and Braulke, 2009; Mole et al., 2011).

Here, we focus on two NCL diseases: classic infantile NCL (CLN1) and late infantile variant NCL (CLN5), which are caused by mutations in *CLN1* and *CLN5* genes, respectively (Vesa et al., 1995; Savukoski et al., 1998; Kousi et al., 2012). *CLN1* encodes for PPT1, a soluble lysosomal enzyme that is involved in depalmitoylation of proteins (Camp and Hofmann, 1993), although the *in vivo* substrates of PPT1 are currently unknown (Hellsten et al., 1995; Jalanko and Braulke, 2009). The *CLN5* gene encodes a soluble lysosomal glycoprotein, implicated recently in endosomal sorting (Schmiedt et al., 2010; Mamo et al., 2012). CLN5 protein colocalizes with lysosomal-associated membrane protein (LAMP-1) (Vesa et al., 2002; Schmiedt et al., 2010), and is expressed by both neurons and glia (Holmberg et al., 2004; Schmiedt et al., 2012).

We have previously generated *Cln1* and *Cln5* knockout (ko) mouse models (Jalanko et al., 2005; Kopra et al., 2004). The *Cln1* ko mouse model presents with a severe neurodegenerative disease, whereas *Cln5* ko mice have a much milder phenotype that progresses more slowly. Both of these mice suffer from several neurological defects, including motor dysfunction, and exhibit progressive weight loss and brain atrophy. Neuropathological analyses show progressive accumulation of autofluorescent storage material, and a marked glial activation, which precedes neuronal loss and is most pronounced in the thalamocortical system. Gene expression profiling of cortical tissue revealed common affected pathways in *Cln1* ko and *Cln5* ko mouse models, including inflammation, cytoskeleton integrity and the neuronal growth cone assembly (von Schantz et al., 2008). Molecular interaction studies of NCL proteins have shown that CLN5 appears to interact with other NCL proteins *in vitro*, including CLN1/PPT1, CLN2 (tripeptidyl-peptidase 1, TPP1), CLN3, CLN6 and CLN8 (Vesa et

[1]National Institute for Health and Welfare, Public Health Genomics Unit, Helsinki, Finland
[2]Institute for Molecular Medicine Finland, FIMM, Biomedicum Helsinki, Helsinki, Finland
[3]Pediatric Storage Disorders Laboratory, Department of Neuroscience and Centre for the Cellular Basis of Behaviour, James Black Centre, King's Health Partners Centre for Neurodegeneration Research, Institute of Psychiatry, King's College London, London, UK
[4]Finnish Medicines Agency, Helsinki, Finland and University of Helsinki, Helsinki, Finland
*Author for correspondence (anu.jalanko@thl.fi)

Received 30 April 2012; Accepted 10 October 2012

TRANSLATIONAL IMPACT

Clinical issue

Neuronal ceroid lipofuscinoses (NCLs) are monogenic neurodegenerative diseases that offer well-established models with which to study the molecular events underlying neurodegeneration. Although there are at least ten different genes that underlie NCLs, the clinical phenotype is usually similar, and is generally characterized by progressive loss of vision, mental and physical decline, epileptic seizures and premature death. The similar phenotypes observed between genetically different NCL mouse models, and the potential for interactions between different NCL proteins, suggest that shared or convergent disease mechanisms might underlie the different forms of the disease. Analysis of these disease mechanisms should help to identify biomarkers that could be used to monitor the efficacy of therapeutic strategies. No curative therapies for NCLs are currently available, but several promising approaches are being investigated, particularly for the forms of the disease caused by deficiency of soluble lysosomal proteins such as CLN1 and CLN5, which were investigated in this study.

Results

The authors developed a mouse model lacking both *Cln1* and *Cln5* genes to study disease mechanisms in the NCLs. The consequences of combined deficiency of CLN1 and CLN5 are of interest because these proteins might interact, and common disease mechanisms have been suggested. The authors show that deficiency of both *Cln1* and *Cln5* genes leads to a more severe NCL phenotype in mice than does deficiency of either gene alone. Cortical demyelination, and pronounced glial activation in cortical and thalamic regions, was followed by cortical neuron loss. Specifically, microglial activation and lipid abnormalities were highlighted. The authors also identified several dysregulated proteins that might have value as biomarkers. Finally, the authors show that expression of α-synuclein was decreased in the brains of *Cln1/5* double-knockout mice, an interesting finding that warrants further investigation.

Implications and future directions

This study demonstrates the use of a new *Cln1/5* double-knockout mouse for identifying disease-modifying factors in NCL and other neurodegenerative diseases. Further studies using this model will help to more accurately identify the molecular defects underlying NCLs associated with CLN1 or CLN5 mutations, and to identify disease biomarkers. Deeper understanding of the biochemical and molecular cascade of events relevant to the pathogenesis of NCLs will be required to achieve significant therapeutic outcomes.

al., 2002; Lyly et al., 2009). In addition, CLN1 and CLN5 share a common interaction partner, the F1 subunit of ATP synthase, which modulates the lipid homeostasis in neurons (Lyly et al., 2008; Lyly et al., 2009).

The finding that similar functional pathways are affected in these forms of NCL and the potential interaction of CLNs at the protein level, raise the possibility that NCL diseases might also be linked at a molecular level. To gain a deeper insight into the shared molecular and pathological events behind the NCLs and the underlying mechanisms of neurodegeneration, we developed a double-knockout mouse model lacking both *Cln1* and *Cln5* genes (*Cln1*/*5* dko). These mice were first analyzed for the possible defects in embryonic development using induced pluripotent stem (iPS) cell technology. In the brain, the accumulation of autofluorescence storage material, presence of astrocytosis, microglial activation and signs of myelination defects were also investigated and stereological analyses were performed to study brain atrophy and neuronal loss. This analysis focused upon the onset and progression of thalamic and cortical neuron loss, based on the changes we have documented in mice singly deficient for either *Cln1* or *Cln5* (Kopra et al., 2004; Jalanko et al., 2005).

Because previous studies have suggested that CLN1 and CLN5 proteins and diseases are closely related and linked to changes in cellular lipid homeostasis (Lyly et al., 2008; Schmiedt et al., 2012), we also conducted plasma lipid profiling of *Cln1/5* dko mice. Finally, gene expression profiling of the *Cln1/5* dko mouse cortex was performed in order to reveal the functional pathways that might be shared by CLN1 and CLN5 diseases.

RESULTS

Cln1/5 dko iPS cells show impaired embryoid body formation and delayed differentiation potential

The *Cln1/5* dko offspring were viable and fertile. However, the cross-breeding of *Cln1* ko and *Cln5* ko mice produced fewer double homozygous *Cln1/5* dko offspring than expected according to Mendelian ratios (supplementary material Table S1), when the parents were homozygous for one of the alleles and heterozygous or homozygous for the other allele. To study a possible defect in breeding or early development of *Cln1/5* dko mice in more detail, we generated several iPS cell lines from *Cln1/5* dko and wild-type mouse embryonic fibroblasts (MEFs). Two wild-type (clones 15 and 23) and three different *Cln1/5* dko (clones 3, 19-2 and 20) iPS cell clones were selected for further experiments on the basis of their positive expression of embryonic stem (ES) cell markers SSEA-1, *Nanog*, *Rex-1*, *Fgf-4*, *Esg-1* and *E-ras* (supplementary material Fig. S1) and their differentiation potential into embryonic germ layers (supplementary material Fig. S2). Equal numbers of feeder-free cells from wild-type and *Cln1/5* dko iPS clones were plated in parallel for embryoid body (EB) formation and the experiment was repeated three times with different clones. Daily microscopic analyses of growing EBs showed that between days two and seven the *Cln1/5* dko EBs were consistently smaller and more irregularly shaped than the wild-type EBs (Fig. 1A, an example of one experiment). Furthermore, the total number of EBs formed from *Cln1/5* dko iPS cell clones appeared to be smaller than those from wild-type clones. Calculation of the diameter of 7-day-old EBs in different clones revealed that this reduction in EB size was also statistically significant (Fig. 1B). This finding was consistent across three different *Cln1/5* dko iPS cell clones. From day seven onwards, both the size and the shape of EBs became more similar between the *Cln1/5* dko and wild type, indicating problems in early development of EBs (data not shown). The formed EBs were then plated on gelatin-coated plates to allow spontaneous differentiation and cell outgrowth from EBs. Microscopic analyses showed that cellular outgrowth from *Cln1/5* dko EBs was much slower than from the wild-type EBs. On day three after plating, wild-type EBs had lost their round shape and cellular growth was seen all over the plates. In contrast, *Cln1/5* dko EBs were still round and cellular growth was only detected close to the EBs (Fig. 1C), indicating that spontaneous cell differentiation was also delayed. These possible defects in early development could explain the detected decrease in the number of the born offspring of *Cln1/5* dko mice.

Cln1/5 dko mice display an early neuropathological phenotype

The *Cln1/5* dko mice presented with a rapidly progressing NCL disease phenotype, already displaying severe symptoms, including seizures and motor dysfunction, by the age of 3 months, which was

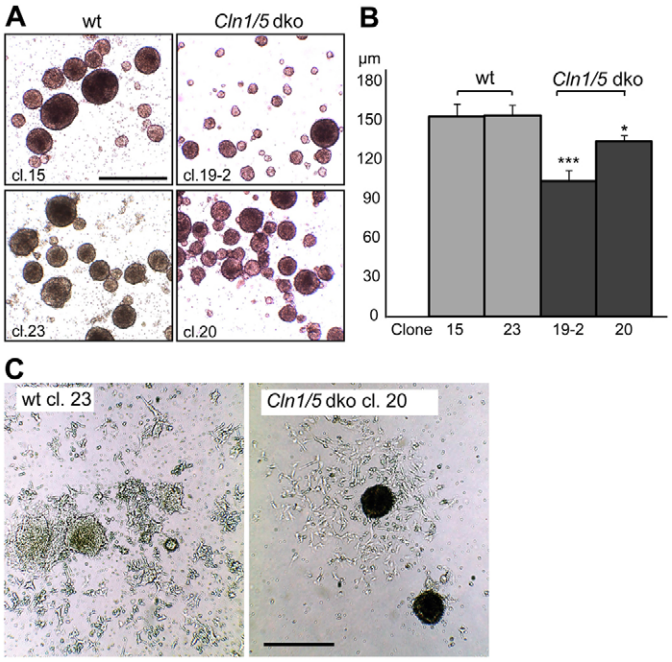

Fig. 1. Impaired EB formation and differentiation of *Cln1/5* dko iPS cells. (A) Microscopic images reveal the smaller size and more irregular shape of *Cln1/5* dko EBs compared with wild-type EBs on day seven. (B) Statistical analysis of EB diameters shows significant difference in the EB size of wild-type and *Cln1/5* dko clones. Columns present average EB size ($n \geq 40$); error bars represent s.e.m. *$P<0.05$, ***$P<0.001$. (C) EBs from 7-day-old mice were plated on gelatin-coated plates for spontaneous differentiation. Images show slower cellular outgrowth from *Cln1/5* dko EBs compared with wild-type EBs, indicating delayed spontaneous differentiation potential of *Cln1/5* dko EBs. Images were taken 3 days after plating. Scale bars: 500 µm.

much earlier than *Cln1* ko mice (5 months) or *Cln5* ko mice (8 months) (Jalanko et al., 2005; Kopra et al., 2004) (data not shown). The onset of the symptoms and the progression of the disease were slightly variable among the *Cln1/5* dko mice. All three mouse models showed a significant reduction in body weight at the age of 3 months compared with wild-type controls (supplementary material Fig. S3). *Cln1/5* dko mice were euthanized at the age of 3 months due to their severe disease phenotype.

The accumulation of autofluorescent lipopigments is a key pathological feature of all forms of NCL and was analyzed in *Cln1* ko, *Cln5* ko, *Cln1/5* dko and wild-type control mice via confocal microscopy. Increased amounts of punctate autofluorescent material were observed in the thalamus and cortex of 3-month-old *Cln1* ko, whereas in *Cln5* ko and in wild-type controls it was almost absent at this age. In contrast, *Cln1/5* dko mice displayed a much more pronounced accumulation of autofluorescent material (Fig. 2A), and this was already seen in 1-month-old *Cln1/5* dko mice (data not shown). Thresholding image analysis showed elevated, but not significant, levels of autofluorescent material in the cortex and thalamus of *Cln1* ko and *Cln1/5* dko mice, compared with wild type (Fig. 2B).

The ultrastructural appearance of the storage material is specific to individual forms of NCL and it differs between these forms (Haltia, 2003; Tyynelä et al., 1993; Tyynelä et al., 2004). On a mixed C57BL background, *Cln1* ko mice show accumulation of granular osmiophilic deposits (GRODs) in the brain and other tissues, whereas in *Cln5* ko mice, the storage material displays rectilinear, curvilinear and fingerprint profiles (Jalanko et al., 2005; Kopra et al., 2004). In a C57BL/6JRcc background, the ultrastructure of the storage material in *Cln1* ko mice was composed of GRODs, and in *Cln5* ko the storage material varied from rectilinear to fingerprint-like (Fig. 2C, panels 5 and 6). Electron microscopic analysis of 3-month-old *Cln1/5* dko mouse brains revealed marked accumulation of GRODs within cortical and thalamic neurons (Fig. 2C, panels 1 and 3). The ultrastructure of the storage deposits was almost identical to that seen in *Cln1* ko mice (Fig. 2C, panel 5), but the storage deposits were much more abundant in the dko mice compared with either of the single ko mice. Within cortical neurons, tiny electron-dense grains were visible inside these GRODs (Fig. 2C, panel 2), whereas in the thalamus, the storage bodies appeared to be more electron-dense than in the cerebral cortex (Fig. 2C, panels 3 and 4). Higher magnification shows that the GRODs are surrounded by a double membrane (Fig. 2C, panels 2 and 4).

Early immune response is enhanced in *Cln1/5* dko mice

Localized astrocytosis and microglial activation has been reported to occur both in *Cln1* ko and *Cln5* ko mice (Bible et al., 2004; von Schantz et al., 2009; Schmiedt et al., 2012). To investigate the extent of astrocytosis in *Cln1/5* dko mice we stained brain sections from 3-month-old mice for the astrocytic marker glial fibrillary acidic protein (GFAP), and compared them to *Cln5* ko, *Cln1* ko and wild-type mice at the same age. We concentrated our analysis upon primary somatosensory barrelfield cortex (S1BF) and thalamic ventral posteromedial nucleus/ventral posterolateral nucleus (VPM/VPL), which relays sensory information to this cortical subfield, because both of these structures are consistently severely affected in NCL mouse models (Cooper, 2010). As previously reported (von Schantz et al., 2009), only a few scattered GFAP-positive astrocytes were present in VPM/VPL of young *Cln5* ko mice, but many more intensely stained astrocytes were present in the thalamic nucleus of young *Cln1* ko mice. However, GFAP staining of the corresponding brain region in *Cln1/5* dko mice revealed a more profound astrocytosis, significantly greater than that seen in *Cln5* ko mice and modestly increased compared with *Cln1* ko mice, with the VPM/VPL and surrounding nuclei of *Cln1/5* dko mice completely filled with hypertophic and intensely GFAP-immunoreactive astrocytes (Fig. 3A). Comparing single- and double-knockout mice revealed a similar relationship in degree of staining in the S1BF region of the cortex, showing pronounced astrocytosis all across cortical laminae in *Cln1* ko mice, but with additional bands of more intensely and darkly stained astrocytes in laminae II-IV and VI in *Cln1/5* dko mice (Fig. 3A). Thresholding image analysis confirmed the significant increase in GFAP immunoreactivity in VPM/VPL and S1BF regions of *Cln1* ko and *Cln1/5* dko brains, compared with the wild-type brains (Fig. 3C).

Activated microglia can be detected by the expression of CD68, a lysosomal/endosomal membrane glycoprotein (Holness et al., 1993). In wild-type mice, palely stained CD68-positive microglia were present in most CNS regions, but at 3 months of age widespread CD68 immunoreactivity was present in the brains of

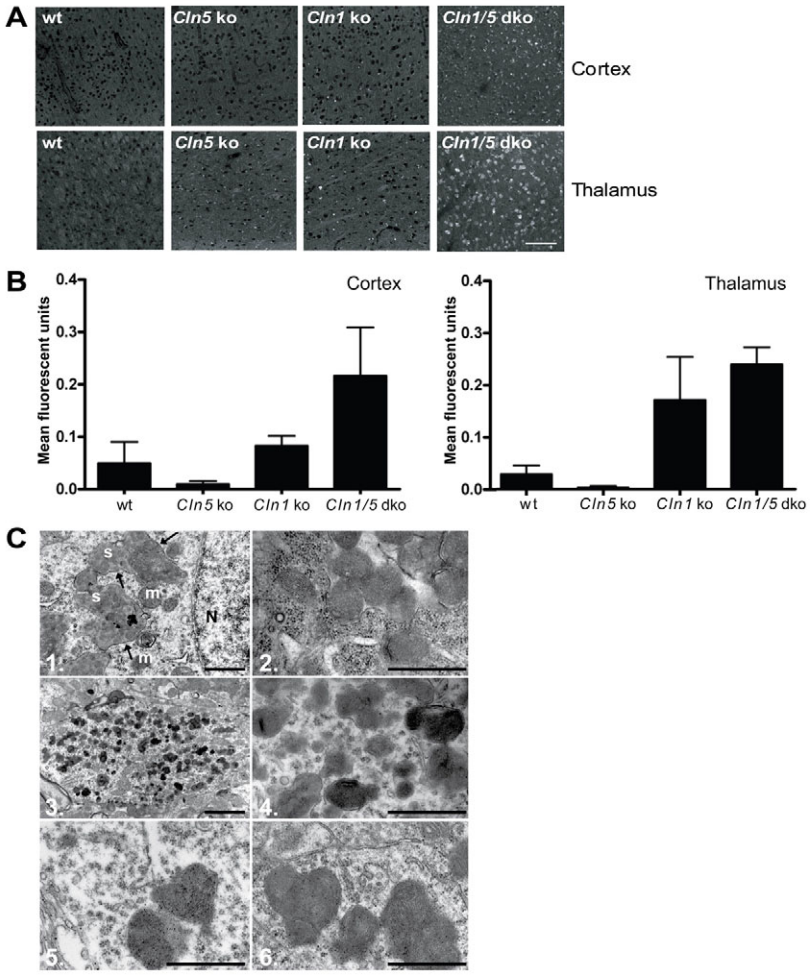

Fig. 2. Accumulation of autofluorescent storage material in cerebral cortex and thalamus. (A) Confocal images of tissue sections from the cortex and thalamus show markedly increased autofluorescence in 3-month-old *Cln1/5* dko mice. Scale bar: 100 µm. (B) Thresholding image analysis revealed higher levels, although not significantly, of autofluorescent storage material in the cortex and thalamus of *Cln1/5* dko mice. (C) Electron micrographs of the storage material in the *Cln1/5* dko, *Cln1* ko and *Cln5* ko brains. (C1) Cortical neuron of 3-month-old *Cln1/5* dko mouse shows numerous storage bodies (indicated by arrows) and mitochondria in the perinuclear area. (C2) At higher magnification, ultrastructure of the neuronal storage material is clearly visible, showing typical granular osmiophilic deposits, GRODs, with tiny grains inside. The storage material is surrounded by a double membrane. (C3) Within the thalamus of 3-month-old *Cln1/5* dko mice, some neurons were loaded with storage bodies, which were more electron-dense than those in the cerebral cortex. (C4) Higher magnification of the thalamic storage bodies shows typical GRODs surrounded by a double membrane. (C5) Ultrastructure of the storage material within cortical neurons of 3-month-old *Cln1* ko mice closely resembles the GRODs seen in the cerebral cortex of *Cln1/5* dko mice, although the storage deposits are less abundant in *Cln1* ko mice than in *Cln1/5* dko mice at this age. (C6) In the cortex of 3-month-old *Cln5* ko mice, the neuronal storage material is composed of membranous profiles with rectilinear and fingerprint-like features. Magnification 10,000× in C1 and C3; 40,000× in C2 and C4-6. Scale bars: 2 µm (C1,C3); 1 µm (C2,C4-C6). s, storage bodies; m, mitochondria; N, nucleus.

all three mutant mice, most notably in the thalamic relay nuclei, lateral and medial geniculate nuclei, cortical regions (S1BF), the subiculum and selected hippocampal subfields, the globus pallidus and substantia nigra. Focusing upon the S1BF and VPM/VPL regions, microglial activation was consistently more advanced in this thalamic relay nucleus than in its corresponding cortical target region (Fig. 3B). Consistent with our recent findings (Schmiedt et al., 2012), 3-month-old *Cln5* ko mice already showed evidence of microglial activation, with CD68-stained microglia displaying larger and more darkly stained cell soma than in wild-type controls. This phenotype was more pronounced in *Cln1* ko mice, with a subset of microglia displaying a brain-macrophage-like morphology, but was exacerbated further in *Cln1/5* dko mice, in which the entire thalamus was filled with intensely stained CD68-positive microglia with swollen cell soma and only very short cell processes (Fig. 3B). An elevated level of CD68 staining was already detectable in both thalamus and cortex of *Cln1/5* dko mice at 1 month of age (supplementary material Fig. S4). Thresholding image analysis verified this widespread and significant microglial activation in the S1BF of *Cln1/5* dko mouse brains, compared with wild-type mice (Fig. 3D). Due to a higher degree of variation, this elevated CD68 expression did not exceed the significant levels of microglial activation in the VPM/VPL or S1BF regions of *Cln5* ko mice that we have previously reported (Schmiedt et al., 2012).

Disturbed cortical myelination in *Cln1/5* dko mice

Disturbed myelination has previously been described in *Cln5* ko mice (Kopra et al., 2004; von Schantz et al., 2009; Schmiedt et al., 2012), but has not been studied in *Cln1* ko mice. Immunostaining for myelin basic protein (MBP), a main protein constituent of the myelin sheath, revealed no overt disruption of white matter structures in 1- and 3-month-old *Cln5* ko mice, but the superficial laminae of S1BF contained fewer MBP-positive fibers (Schmiedt et al., 2012). Performing similar analyses in this study revealed more pronounced effects on MBP staining in this brain region of *Cln1/5* dko mice, compared with either *Cln1* ko or *Cln5* ko mice. Compared with wild-type controls, 1-month-old *Cln1/5* dko mice displayed fewer MBP immunopositive fibers running dorsoventrally and horizontally through the superficial laminae (laminae II and III) of S1BF (Fig. 4A). By 3 months of age, all three mutant mouse models showed fewer MBP-positive fibers in the superficial laminae of S1BF compared with wild-type controls (Fig. 4B).

Cln1/5 dko mice show neuron loss in cortical lamina VI at 3 months of age

Cortical atrophy is a common feature of all human and murine NCLs (Cooper et al., 2006), but occurs relatively late in disease progression. In order to determine whether this phenotype was

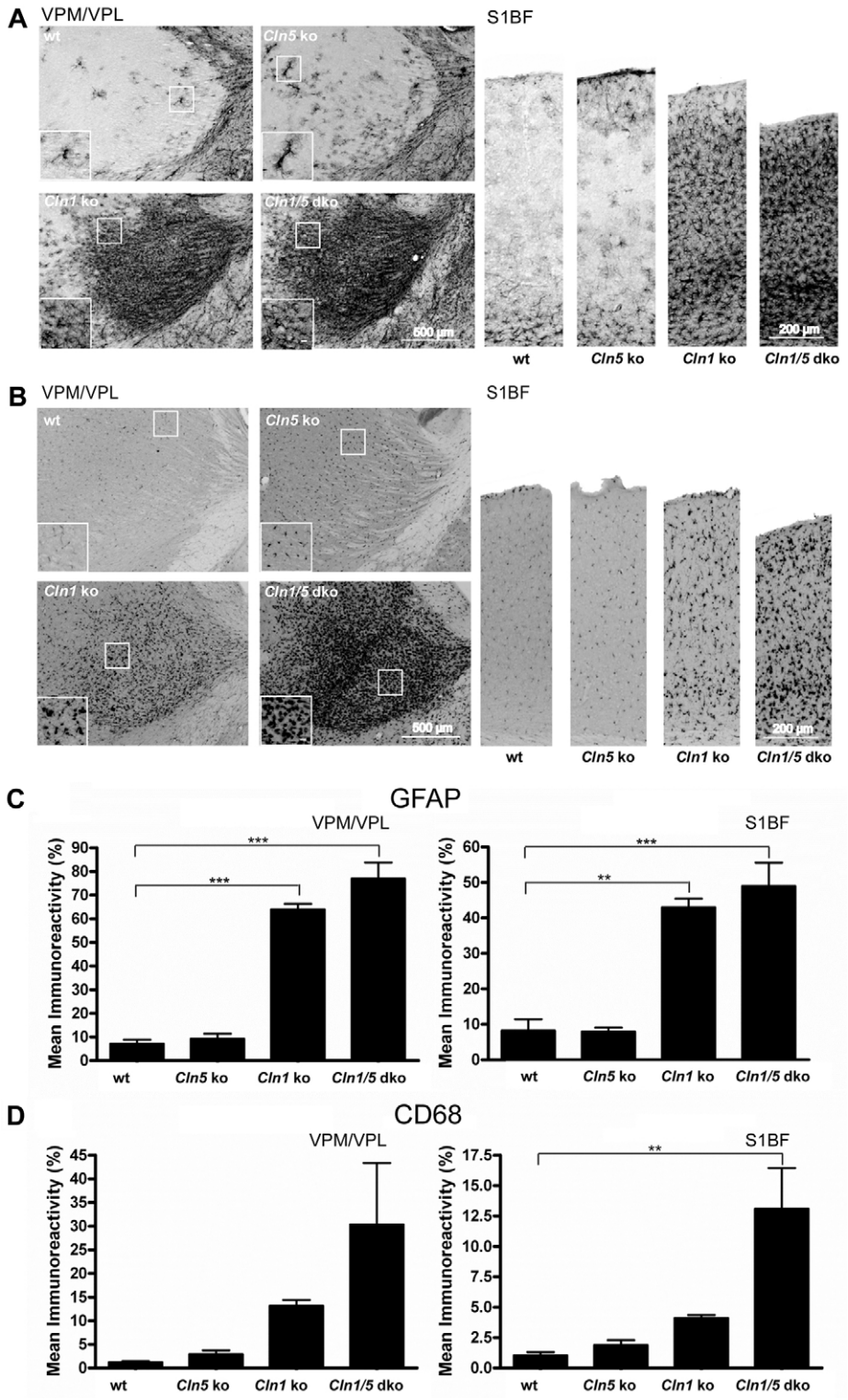

Fig. 3. Increased astrocytosis and widespread microglial activation in the thalamocortical system of 3-month-old *Cln1/5* dko mice.
(A) Immunohistochemical staining for the astrocytic marker GFAP in 3-month-old wild-type, *Cln5* ko, *Cln1* ko and *Cln1/5* dko mice. Representative images from VPM/VPL and S1BF show pronounced and widespread astrocytosis in *Cln1* ko and *Cln1/5* dko brains, and elevated GFAP expression in the *Cln5* ko brain. Insets from *Cln5* ko, *Cln1 ko* and *Cln1/5* dko show the morphology of GFAP-positive hypertrophic astrocytes with enlarged soma and thickened processes.
(B) Immunohistochemical staining for the microglial marker CD68 in 3-month-old wild-type, *Cln5* ko, *Cln1* ko and *Cln1/5* dko mice. Widespread activation of microglia in VPM/VPL and S1BF was evident in all three mouse models, being most elevated in *Cln1* ko and *Cln1/5* dko brains. Insets from *Cln5* ko, *Cln1* ko and *Cln1/5* dko show the morphology of activated CD68-positive microglia, with swollen soma and shortened processes. Scale bars: 50 µm (insets) or as indicated.
(C) Quantification of increased microglial activation (CD68 immunoreactivity) and (D) astrocytosis (GFAP immunoreactivity) in 3-month-old *Cln1/5* dko mice. Thresholding image analysis confirms the significantly increased GFAP expression in the thalamic VPM/VPL and cortical S1BF regions of *Cln1/5* dko mouse brain, compared with wild-type controls. CD68 expression was significantly increased in the S1BF of *Cln1/5* dko mouse brain compared with wild-type brain. Error bars represent s.e.m. $^{**}P<0.01$, $^{***}P<0.001$.

already apparent in 3-month-old *Cln1/5* dko mice, we carried out thickness measurements in Nissl-stained sections through primary motor (M1), S1BF, primary visual (V1) and lateral entorhinal (LEnt) regions, as representative cortical regions that serve different functions. Compared with wild-type controls, no significant thinning was observed in any cortical region of 3-month-old *Cln1/5* dko brains or in age-matched *Cln1* ko mice (supplementary material Fig. S5A). As reported previously (von Schantz et al., 2009), the cortical thickness of S1BF, M1 and V1 in *Cln5* ko mice was significantly increased at this age.

We next conducted a stereological analysis of regional volumes in *Cln1* ko, *Cln5* ko, *Cln1/5* dko and wild-type brains at 3 months

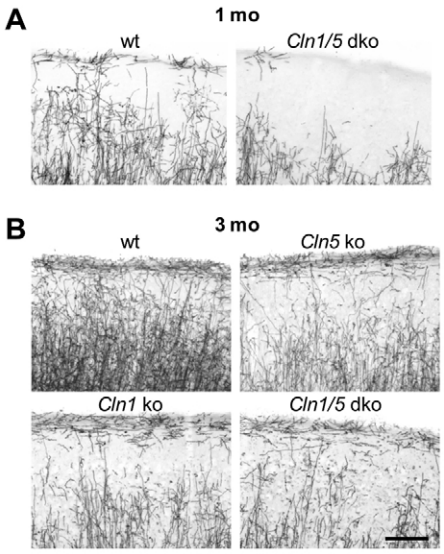

Fig. 4. Defective myelination in the cortical laminae of *Cln5* ko, *Cln1* ko and *Cln1/5* dko mouse brain. (A) Immunohistochemical staining with MBP revealed loss of MBP immunopositivity in *Cln1/5* dko cortex at the age of 1 month, especially in the most superficial laminae of S1BF (laminae II and III). (B) All mouse models showed less MBP immunopositivity in the superficial laminae of S1BF than wild-type mice at the age of 3 months. Scale bar: 100 µm.

of age. Cavalieri estimates of regional volumes revealed no significant atrophy of the cortex or hippocampus of the *Cln1/5* dko mice at this age. Consistent with the thickness measurements, the cortical volumes of *Cln5* ko mice were significantly increased compared with the wild-type controls. In addition, the hippocampal volume was significantly increased in the *Cln5* ko brain (supplementary material Fig. S5B).

To investigate the extent of neuron loss in *Cln1/5* dko mice, we conducted optical fractionator estimates of the number of Nissl-stained VPM/VPL neurons and of neuron populations in three cortical laminae of S1BF: lamina IV granule neurons that receive thalamic innervations; projection neurons in lamina V; and lamina VI neurons that supply feedback to the thalamus. We chose these regions because they are characteristically vulnerable in mouse models of NCL (Pontikis et al., 2005; Weimer et al., 2006; Kielar et al., 2007; Partanen et al., 2008). This analysis revealed consistently fewer neurons in all brain regions of 3-month-old *Cln1/5* dko mice, than in mice deficient for either *Cln1* or *Cln5* alone. However, it was only in lamina VI of S1BF of 3-month-old *Cln1/5* dko mice that this neuron loss was statistically significant (Fig. 5).

Lipid profiles in *Cln1/5* dko mice plasma show significant increase in phospholipids and PLTP activity

Alterations in systemic lipid metabolism have been reported in both *Cln1* ko (Lyly et al., 2008) and *Cln5* ko mice (Schmiedt et al., 2012). Therefore, we wanted to assess possible lipid metabolism changes when both *Cln1* and *Cln5* are deleted. Plasma cholesterol, phospholipids, triglycerides, apoA-1 and the activity of phospholipid transfer protein (PLTP) in 1-month-old female mice were analyzed from wild-type, *Cln5* ko, *Cln1* ko and *Cln1/5* dko mice. Phospholipid levels in *Cln1/5* dko mice were significantly increased, whereas cholesterol, triglyceride and apoA-1 levels were slightly elevated compared with wild-type controls (Fig. 6A). Total cholesterol levels were significantly decreased in *Cln5* ko plasma, as well as in *Cln1* ko plasma, as reported previously (Lyly et al., 2008). However, in this study, the cholesterol levels in *Cln5* ko mice did not significantly differ from those of wild-type mice, as previously reported (Schmiedt et al., 2012). Increased plasma PLTP activity is suggested to be associated with increased cholesterol levels (Colhoun et al., 2001), and PLTP activity was

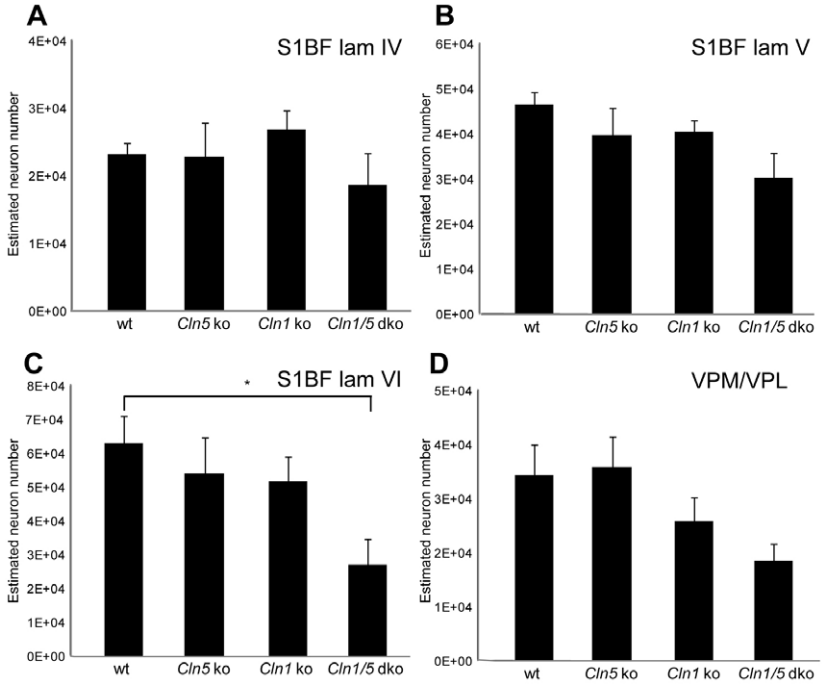

Fig. 5. Early loss of cortical neurons in *Cln1/5* dko mice. Unbiased optical fractionator estimates of the number of Nissl-stained neurons of 3-month-old mice in S1BF lamina IV (A), lamina V (B), lamina VI (C) and VPM/VPL (D) revealed significant loss of neurons in S1BF lamina VI of *Cln1/5* dko brain. No significant loss of cortical S1BF neurons in laminae IV and V, or thalamic VPL/VPL neurons, was observed. *P<0.05.

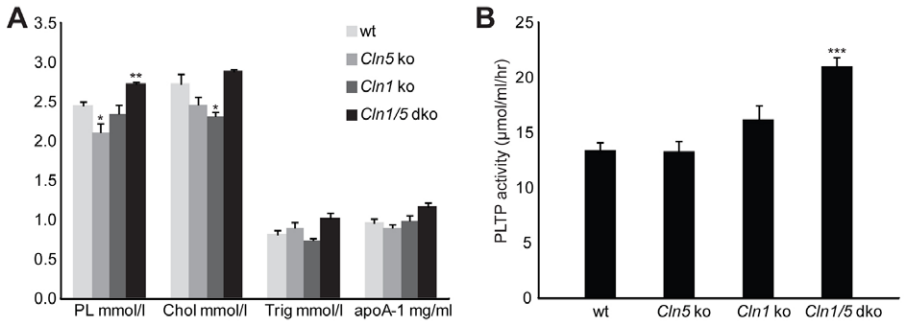

Fig. 6. Lipid profile analysis from 1-month-old wild-type, *Cln1* ko, *Cln5* ko and *Cln1/5* dko mouse plasma. Cholesterol (Chol), phospholipid (PL), triglyceride (Trig) and apoA-1 levels (A) and PLTP activity (B) were determined from individual wild-type, *Cln1* ko, *Cln5* ko and *Cln1/5* dko mouse plasma samples. PL levels, as well as PLTP activity, were significantly increased in *Cln1/5* dko mice. Values plotted as mean + s.e.m. **P*<0.05, ***P*<0.01, ****P*<0.001.

indeed significantly increased in *Cln1/5* dko mice compared with wild-type mice (Fig. 6B). However, plasma PLTP activity in *Cln1* ko and *Cln5* ko mice did not differ from that of wild-type controls and therefore did not support our previous results (Lyly et al., 2008; Schmiedt et al., 2012).

To verify the detected lipid changes in *Cln1/5* dko mice, we also analyzed the distribution of lipids and apoA-1 in lipoprotein fractions. Cholesterol levels were clearly elevated in high density lipoprotein (HDL) particles and slightly decreased in very low density lipoprotein (VLDL) particles of *Cln1/5* dko plasma (supplementary material Fig. S6A). In addition, the elevated PLTP activity led to enhanced phospholipid transfer from the VLDL pool to HDL pool (supplementary material Fig. S6A). ApoA-1 was clearly elevated in both small (pre-β-HDL) and large HDL particles (supplementary material Fig. S6B), indicating increased PLTP activity, which is known to induce the formation of lipid-poor pre-β-HDL particles (Siggins et al., 2007). Furthermore, elevated triglyceride levels were found in VLDL particles (supplementary material Fig. S6C). Together, these results suggest a change in systemic lipid homeostasis in *Cln1/5* dko mice.

Gene expression profiling of the *Cln1/5* dko mouse cortex

Global gene expression analysis of ~45,000 transcripts from 1-month-old *Cln1/5* dko cortex revealed statistically significant upregulation of 24 genes (Table 1) and downregulation of 31 genes (Table 2). The most upregulated gene was cyclase-associated protein 1 (*Cap1*, 1.9-fold), and the most downregulated gene was α-synuclein (*Snca*, –177.2-fold). Other upregulated genes included complement subcomponents C1qb (*C1qb*, 1.6-fold) and C1qc (*C1qc*, 1.4-fold), Fc receptor homolog S (*Fcrls*, 1.6-fold) and glial

Table 1. Upregulated genes in 1-month-old *Cln1/5* dko cortex

Probe ID	Symbol	Description	Adj. *P*-value	FC
3440343	*Cap1*	CAP, adenylatecyclase-associated protein 1 (yeast)	2.88E-03	1.9
580332	*C1qb*	Complement component 1, q subcomponent, beta polypeptide	5.87E-03	1.6
940541	*Fcrls*	Fc receptor-like S, scavenger receptor	3.03E-02	1.6
1450139	*Gfap*	Glial fibrillary acidic protein	1.63E-03	1.5
3710170	*C1qc*	Complement component 1, q subcomponent, C chain	3.03E-02	1.4
2710367	*Ntsr2*	Neurotensin receptor 2	2.68E-02	1.4
2630543	*Ndrg2*	N-myc downstream regulated gene 2	1.79E-03	1.4
6110736	*B2m*	Beta-2 microglobulin	1.38E-02	1.4
5570253	*B2m*	Beta-2 microglobulin	1.58E-02	1.3
7150026	*Fam171b*	Family with sequence similarity 171, member B	1.66E-02	1.3
940338	*S100a1*	S100 calcium binding protein A1	1.25E-02	1.3
6350044	*Slc2a1*	Solute carrier family 2 (facilitated glucose transporter), member 1	2.14E-02	1.3
2650672	*Mll1*	Myeloid/lymphoid or mixed-lineage leukemia 1	3.89E-02	1.2
7050487	*Cd63*	CD63 antigen	2.24E-02	1.2
5670328	*Atp1b2*	ATPase, Na+/K+ transporting, beta 2 polypeptide	3.89E-02	1.2
2340349	*Aldh2*	Aldehyde dehydrogenase 2, mitochondrial	3.89E-02	1.2
3190301	*Aak1*	AP2 associated kinase 1	2.88E-02	1.1
1300327	*Capzb*	Capping protein (actin filament) muscle Z-line, beta	3.21E-02	1.1
1170768	*Cox6a1*	Cytochrome c oxidase, subunit VI a, polypeptide 1	3.03E-02	1.1
6180465	*Ddx17*	DEAD (Asp-Glu-Ala-Asp) box polypeptide 17	4.11E-02	1.1
1510133	*Cox6a1*	Cytochrome c oxidase, subunit VI a, polypeptide 1	3.43E-02	1.1
2570669	*Mapk1*	Mitogen-activated protein kinase 1	3.51E-02	1.1
620470	*Gm10224*	Predicted pseudogene 10224	3.66E-02	1.1
4060274	*Dlgap1*	Discs, large (*Drosophila*) homolog-associated protein 1	4.91E-02	1.1

FC, fold change; Adj. *P*-value, adjusted *P*-value.

Table 2. Downregulated genes in 1-month-old *Cln1/5* dko cortex

Probe ID	Symbol	Description	Adj. *P*-value	FC
5130372	*Snca*	Synuclein, alpha	0.00E+00	–177.2
5130202	*Snca*	Synuclein, alpha	0.00E+00	–84.4
730372	*Snca*	Synuclein, alpha	1.18E-03	–7.3
990064	*Ppt1*	Palmitoyl-protein thioesterase 1	1,31E-02	–5,1
380259	*Mal*	Myelin and lymphocyte protein, T cell differentiation protein	3.50E-02	–1.6
4780010	*Mal*	Myelin and lymphocyte protein, T cell differentiation protein	3.76E-03	–1.6
160465	*Mag*	Myelin-associated glycoprotein	1.24E-03	–1.6
6760255	*Evi2a*	Ecotropic viral integration site 2a	3.21E-02	–1.6
6400053	*Mog*	Myelin oligodendrocyte glycoprotein	3.50E-02	–1.5
290044	*Gamt*	Guanidinoacetatemethyltransferase	4.46E-02	–1.5
620070	*Mog*	Myelin oligodendrocyte glycoprotein	1.28E-02	–1.5
2570228	*Ugt8a*	UDP galactosyltransferase 8A	3.89E-02	–1.5
4120360	*Tspan2*	Tetraspanin 2	1.25E-02	–1.5
2810706	*Fa2h*	Fatty acid 2-hydroxylase	1.83E-02	–1.4
1850435	*Cldn11*	Claudin 11	2.72E-03	–1.4
6940079	*Cnp*	2,3-Cyclic nucleotide 3 phosphodiesterase	2.14E-02	–1.4
3180750	*Dbp*	D site albumin promoter binding protein	1.51E-02	–1.4
6180411	*Gltp*	Glycolipid transfer protein	3.50E-02	–1.3
7040044	*Trf*	Transferrin	3.89E-02	–1.3
1770468	*Adssl1*	Adenylosuccinatesynthetase-like 1	2.69E-02	–1.3
4490554	*Sema4a*	Sema domain, Ig domain, TM domain and semaphorin domain 4A	4.77E-02	–1.3
6960026	*Dbndd2*	Dysbindin (dystrobrevin binding protein 1) domain containing 2	5.35E-04	–1.2
1780221	*Plp1*	Proteolipid protein (myelin) 1	2.72E-03	–1.2
7000343	*Lass2*	LAG1 homolog, ceramide synthase 2	3.89E-02	–1.2
1450646	*Mbp*	Myelin basic protein	3.50E-02	–1.2
2900291	*Nudc*	Nuclear distribution gene C homolog (Aspergillus)	3.66E-02	–1.2
5050577	*Ctps*	Cytidine 5-triphosphate synthase	2.14E-02	–1.2
6620603	*Tecr*	*Trans*-2,3-enoyl-CoA reductase	1.51E-02	–1.2
3420538	*Degs1*	Degenerative spermatocyte homolog 1 (Drosophila)	3.89E-02	–1.1
830397	*Ptn*	Pleiotrophin	3.66E-02	–1.1
7610246	*Slitrk5*	SLIT and NTRK-like family, member 5	3.57E-02	–1.1

FC, fold change; Adj. *P*-value, adjusted *P*-value.

fibrillary acidic protein (*GFAP*, 1.5-fold). Downregulation of oligodendrocytic myelin and paranodal and inner loop protein (*Opalin*, –1.8-fold), as well as other myelin genes (myelin and lymphocyte protein *Mal*, –1.6-fold; myelin associated glycoprotein *Mag*, –1.6-fold; myelin oligodendrocyte glycoprotein *Mog*, –1.5-fold; proteolipid protein *Plp1*, –1.2-fold; and myelin basic protein *Mbp*, –1.2-fold) was also observed. The *Ppt1* (*Cln1*) gene was also downregulated (–5.1-fold), whereas downregulation of the *Cln5* gene was not observed, due to the lack of a specific probe in the gene expression array.

Analyses of biological pathways are often more informative than single gene changes. In order to characterize the affected pathways in 1-month-old *Cln1/5* dko mice, and to compare them to the existing data from *Cln1* ko and *Cln5* ko mice, we performed a DAVID functional annotation clustering analysis. We discovered that pathways related to the immune response were upregulated, whereas pathways related to myelin ensheathment and transmission of nerve impulse were downregulated (Table 3). These results are in line with the published defects in nerve ensheathment and myelination, and upregulation of inflammation-associated pathways in *Cln1* ko mice and neurons (Ahtiainen et al., 2007; von Schantz et al., 2008). A common gene upregulated in all three models (*Cln1* ko, *Cln5* ko and *Cln1/5* dko) is *Cap1*, a gene crucial for the neuronal growth cone-cytoskeletal dynamics (Ahtiainen et al., 2007; von Schantz et al., 2008; this study). Our results from immunohistochemical studies indicate enhanced glial activation and defective myelination in *Cln1/5* dko brain, and are thus consistent with the gene expression analysis data.

The downregulation of the most differentially expressed gene between the two genotypes (wild-type and *Cln1/5* dko), *Snca*, was further evaluated with quantitative real-time reverse-transcriptase PCR (RT-PCR). The results support the microarray data, demonstrating almost complete lack of *Snca* expression in the *Cln1/5* dko cortex (supplementary material Fig. S7A).

Decreased α-synuclein expression in *Cln1/5* dko mouse cortex

As a novel finding, gene expression profiling indicated a pronounced downregulation of α-synuclein gene expression in the *Cln1/5* dko

Table 3. Up- and downregulated pathways in 1-month-old *Cln1/5* dko cortex

Ontology	Genes	Benjamini*	*P*-value	FC
Upregulated pathways				
MHC class I protein complex	5	2.43E-03	1.68E-05	31
MHC protein complex	5	3.22E-03	4.44E-05	25
Defense response	11	1.35E-02	2.35E-05	5
Antigen processing and presentation of peptide antigen via MHC class	4	1.46E-02	5.11E-05	53
Downregulated pathways				
Myelin sheath	3	7.27E-03	1.67E-04	−145.4
Transmission of nerve impulse	7	1.97E-02	1.50E-05	−12.3

*Benjamini-Hochberg method was used for multiple hypothesis testing correction of the *P*-values. FC, fold change.

mouse cortex. To validate this result at the protein level, we performed western blotting of cortical and cerebral (whole brain apart from the cerebellum) lysates from 1- and 3-month-old mice. In cortical lysates from 3-month-old *Cln1/5* dko mice, the expression of full-length (19 kDa) α-synuclein was completely absent compared with wild-type controls (Fig. 7A). In the cerebrum, the expression of α-synuclein protein was absent in three out of five *Cln1/5* dko lysates, whereas two out of five had normal α-synuclein levels (Fig. 7B). Similarly, no expression of α-synuclein was observed in the 1-month-old *Cln1/5* dko mouse cortex (supplementary material Fig. S7B) and expression was reduced in the cerebrum of *Cln1/5* dko mice (supplementary material Fig. S7B). Quantification of α-synuclein expression levels showed significant reduction in α-synuclein expression in both cortex and cerebrum of 1- (supplementary material Fig. S7D) and 3-month-old (Fig. 7C) *Cln1/5* dko mice compared with wild-type controls. The cerebrum of 1- and 3-month-old *Cln1* ko and *Cln5* ko mice expressed unchanged α-synuclein levels (supplementary material Fig. S8).

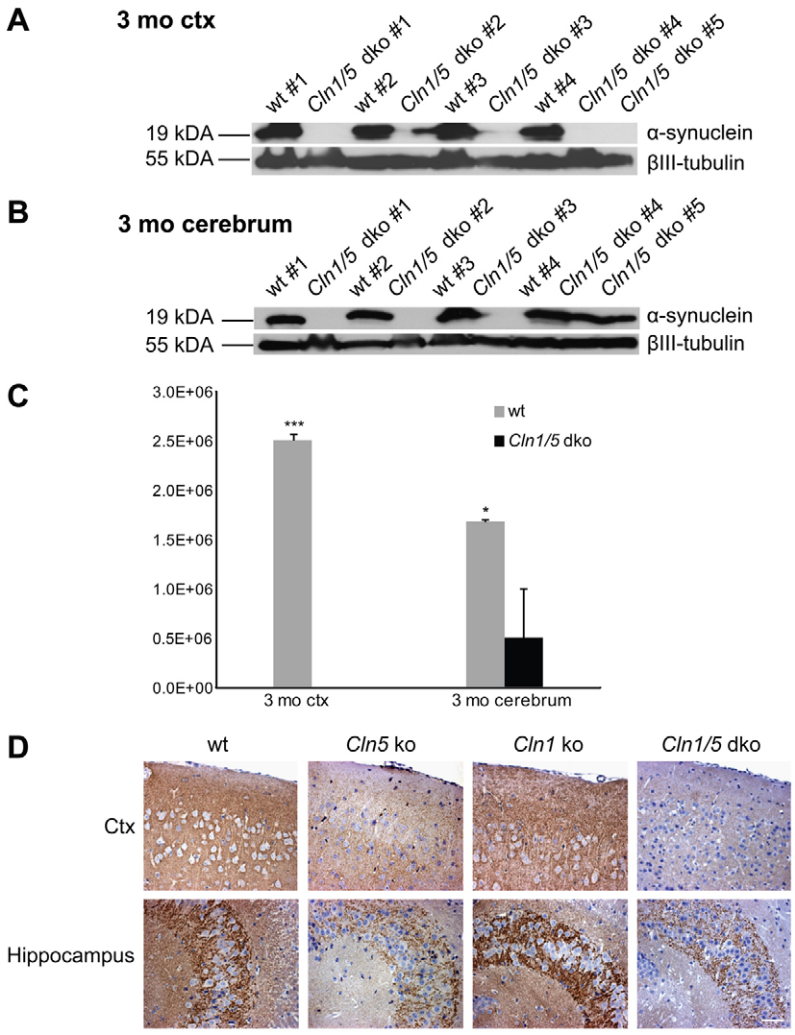

Fig. 7. Western blot analysis of α-synuclein levels in 3-month-old wild-type and *Cln1/5* dko mouse brain. (A) In the cortex, α-synuclein protein expression was completely absent in *Cln1/5* dko brains compared with wild-type brains. (B) α-Synuclein expression in cerebral lysates was absent in three out of five *Cln1/5* dko samples. (C) Quantification of α-synuclein protein expression. Densitometric analysis shows a significant decrease in the expression of α-synuclein in the *Cln1/5* dko cortex and cerebrum compared with the wild-type brains. (D) Immunohistochemical analysis of α-synuclein in 3-month-old wild-type, *Cln1* ko, *Cln5* ko and *Cln1/5* dko brains. There was a marked reduction in α-synuclein staining in the neuropil of *Cln1/5* dko cerebral cortex. Hippocampal α-synuclein staining was also decreased in the *Cln1/5* dko brain. In addition, slightly reduced α-synuclein staining was observed in the cortical neuropil and hippocampus of the *Cln5* ko brain. Scale bar: 50 µm. *P<0.05, ***P<0.001.

Table 4. Overview of neurological and neuropathological changes in *Cln1* ko, *Cln5* ko and *Cln1/5* dko mouse models

Parameter	*Cln1* ko	*Cln5* ko	*Cln1/5* dko
Onset of symptoms	5 months	8 months	3 months
Phenotype	Motor abnormalities, seizures[a]	Motor abnormalities, seizures[b]	Motor abnormalities, seizures[e]
Ultrastructure of storage material	GROD[a]	Rectilinear, curvilinear, fingerprint[b]	GROD[e]
Onset of neuron loss	Thalamus (4 months)[c]	Cortex lam IV and V (4 months)[c]	Cortex lam VI (3 months)[e]
Onset of glial activation	Cortex and thalamus (3 months)[a]	Cortex and thalamus (3 months)[d]	Cortex and thalamus (1 month)[e]
Onset of myelination defects	Cortex (3 months)[e]	Cortex (1 month)[d]	Cortex (1 month)[e]

[a]Jalanko et al., 2005 and unpublished; [b]Kopra et al., 2004 and unpublished; [c]von Schantz et al., 2009; [d]Schmiedt et al., 2012; [e]this study.

α-synuclein protein expression levels were also investigated by immunohistochemical staining in 3-month-old wild-type, *Cln1* ko, *Cln5* ko and *Cln1/5* dko brain sections (Fig. 7D). We observed markedly reduced α-synuclein staining in the cortical neuropil, as well as some reduction in the hippocampus of *Cln1/5* dko mice. In *Cln5* ko mice, cortical and hippocampal α-synuclein immunoreactivity was also somewhat reduced. These results support our western blot findings that show weak α-synuclein expression in the cortex and close to normal expression levels in the cerebrum of a subset of *Cln1/5* dko mice.

DISCUSSION

Characterization of NCL mouse models is essential for obtaining new information about disease progression and for a better understanding of the mechanisms behind the disease. In this study, we have created a new *Cln1/5* dko mouse model and provide a detailed description of neuropathological events, focusing on the consequences of a deficiency in both of these genes. In general, the *Cln1/5* dko mice exhibit an earlier onset and more severe neurological and neuropathological phenotypes than was seen in the individual *Cln1* ko or *Cln5* ko mouse models (summarized in Table 4).

Possible developmental defects are associated with *Cln1/5* deficiency

Despite their severe neurological phenotype, the *Cln1/5* dko mice are viable, but produce fewer double homozygous offspring than expected according to Mendelian ratios, probably due to reduced fertility. Furthermore, our data show that EB formation of *Cln1/5* dko mice iPS cells is impaired, and further differentiation of EBs is much slower than that of wild-type controls. This could indicate that simultaneous deficiency of *Cln1* and *Cln5* genes might impact fetal survival in mice, seen as a lower number of offspring. Indeed, similar findings have previously been shown to be specifically associated with the iPS cells derived from another lysosomal storage disease, mucopolysaccharidosis VII (Meng et al., 2010). Homozygous mutations of both *Cln1* and *Cln5* genes in human patients have not been reported, but CLN1 patients with homozygous mutation of *Cln1* gene accompanied by an extra heterozygous mutation in the *Cln5* gene are known (Kousi, 2012). Our results indicate that the simultaneous dysfunction of both *Cln1* and *Cln5* genes worsens the clinical picture in mice, and *in vitro* experiments also suggest partial lethality. Considering these data, it is possible that the homozygous mutations in both *CLN1* and *CLN5* genes might be lethal in humans and therefore might not be detected in analyses of NCL disease-causing mutations.

Glial activation and defective myelination precede neurodegeneration in *Cln1/5* dko brain

Astrocytosis has long been considered a hallmark of neurodegenerative changes. Significant upregulation of GFAP is evident in immunohistochemistry and microarray studies of *Cln1* ko and *Cln5* ko mice (Elshatory et al., 2003; von Schantz et al., 2008; von Schantz et al., 2009). Our current data are consistent with these findings, with increased levels of astrocytosis in every region of the *Cln1/5* dko mice CNS, which is already strong at the age of 3 months. Microglial activation was also widespread in 3-month-old *Cln1/5* dko CNS, and was especially pronounced in the thalamocortical system. Microglia are the brain's intrinsic immune cells and play important roles in injury and neurodegenerative diseases (Perry et al., 2010). Microglia serve as damage sensors, and injury or pathological processes lead to activation of these cells from their resting state. Thus, this microglial activation in *Cln1/5* dko might be a response to increased cellular damage caused by storage material accumulation and lysosomal enlargement.

Reactive astrocytes and microglia often accompany neuronal loss and might be indicative of neuronal dysfunction (Gehrmann et al., 1995; Macauley et al., 2011). Indeed, in mouse and large animal models of NCL, glial activation invariably precedes neuron loss and is the most accurate predictor of where neurons are subsequently lost (Cooper, 2010). In this respect, the more enhanced reactive phenotype of *Cln1/5* dko mice suggests that neuron loss would also be more pronounced if these mice were allowed, or able, to survive longer. Our investigation of neuron survival in these mice does reveal an earlier onset of neuron loss, although this did not reach significance in most brain regions. Nevertheless, it is evident that deficiency of both *Cln1* and *Cln5* clearly exacerbates this characteristic and early neuropathological feature of NCL disease progression.

Neuron loss begins in cortical lamina VI in *Cln1/5* dko mice

In the *Cln1* ko mouse model, neuron loss begins in the thalamus and only subsequently occurs in the corresponding cortical region (von Schantz et al., 2009). In contrast, in *Cln5* ko mice, neuron loss begins in the cortex and only subsequently occurs in thalamus (von Schantz et al., 2009). In *Cln1/5* dko, the only significant neuron loss was observed in cortical lamina VI of S1BF, suggesting that, as in *Cln5* ko mice, neuron loss in the thalamocortical system of *Cln1/5* dko mice also occurs first in the cortex at the age of 3 months of age. It is perhaps surprising that more pronounced neuron loss was not seen in these *Cln1/5* dko mice, but it should be remembered that this is the earliest documented incidence of significant neuron loss in one of these mouse models and has already occurred at a relatively

young age. It is likely that neuron loss would become far more pronounced if these mice were to survive longer, especially given the profound nature of the exacerbated glial response they display.

In our study, no significant thinning of *Cln1/5* cortex was seen at the age of 3 months. However, *Cln5* ko mice did display a significantly increased thickness in the S1BF, M1 and V1 at this age. Similar findings have been reported previously by von Schantz et al., showing increased thickness in the superficial laminae I-III of 12-month-old *Cln5* ko mice (von Schantz et al., 2009). Similarly, regional volume measurements revealed no atrophy in *Cln1/5* dko brain at the age of 3 months, whereas increased volumes were observed in 3-month-old *Cln5* ko cortex and hippocampus.

Altered lipid and lipoprotein plasma profile in *Cln1/5* dko mice

Previous studies have shown that cholesterol metabolism is disturbed in *Cln1* ko mice (Ahtiainen et al., 2007; Lyly et al., 2008), and more recent studies have indicated even more prominent aberrations in the systemic lipid homeostasis of *Cln5* ko mice (Schmiedt et al., 2012). In this study, we conducted plasma lipid profiling of *Cln1/5* dko mice and observed significantly elevated levels of phospholipids and increased PLTP activity in these mice. These lipid changes were accompanied by the differential distribution of phospholipids and cholesterol in HDL particles. Although the previously published results of plasma lipid analyses of single ko mice were not completely replicated in this study, it is clear that both *Cln1* and *Cln5* ko mice show changes in lipid metabolism. Embryonic neurons of *Cln1* ko mice show highly upregulated synthesis of cholesterol without cholesterol accumulation (Ahtiainen et al., 2007). They also show increased plasma membrane expression of the α- and β-subunits of the F1 complex of the mitochondrial ATP syntase, suggested to function as an apoA-1 receptor (Lyly et al., 2008). Cultured *Cln5* ko macrophages show increased cholesterol efflux as well as changes in sphingolipid trafficking (Schmiedt et al., 2012). In this study, possible changes in lipid metabolism were not assessed at the cellular level. However, plasma lipid changes seen in *Cln1/5* dko mice resemble the trends previously observed in *Cln5* ko mice, whereas *Cln1* ko mice seem to display the opposite changes involving decreased plasma cholesterol (Lyly et al., 2008) (and this study).

Myelin membrane is mainly composed of lipids and is especially enriched in cholesterol, galactolipids and glycosphingolipids (Chrast et al., 2011) and is therefore sensitive to disturbed lipid metabolism. NCL proteins have been suggested to play a role not only in lipid metabolism/transport but also in myelination processes (Schmiedt et al., 2012; Kuronen et al., 2012). Myelination was also affected in this study, as demonstrated by the finding that at the age of 3 months all three mutant mouse models showed fewer MBP-positive fibers in the superficial laminae of S1BF compared with wild-type controls. Although lipid metabolism was not studied in the brain in this study, we postulate that the disturbances in lipid metabolism might affect the assembly of the myelin sheath, leading to defective myelination.

Gene expression profiling of the *Cln1/5* dko cortex implicates changes in genes involved in immune response, nerve ensheathment and transmission of nerve impulse

Gene expression profiling of the *Cln1/5* dko mouse cortex revealed changes in genes involved particularly in immune response, nerve ensheathment and transmission of nerve impulse. Consistent with our immunohistochemical analyses, which indicated defective myelination in the superficial cortical laminae, downregulation of key genes in myelin assembly (*Opalin*, *Mal*, *Mag*, *Mog*, *Plp1* and *Mbp*) was observed. These gene expression changes might be indicative of defects in oligodendrocyte development and function. Furthermore, recent studies have indicated that *Cln5* has a specific role in oligodendrocyte maturation (Schmiedt et al., 2012), and it is possible that these NCLs share both neurodevelopmental and neurodegenerative aspects.

Interestingly, the most downregulated gene in the gene expression data was α-synuclein (*Snca*), which is upregulated in many neurodegenerative diseases, such as Parkinson disease (Vekrellis et al., 2011). *Snca* was also shown to be upregulated in *Cln1* ko embryonic neuronal cell cultures (Ahtiainen et al., 2007). The level of soluble α-synuclein was also significantly reduced in another mouse model of NCL diseases, cathepsin D knockout mice, where the reduced neuropil staining was accompanied by aggregation of α-synuclein in inclusion bodies (Cullen et al., 2009). α-Synuclein is a presynaptic protein and is an important regulator in dopaminergic transmission, synaptic plasticity and vesicle trafficking (Uversky, 2008; Ruipérez et al., 2010). α-Synuclein-deficient mice are viable, but they suffer from significant neurochemical, electrophysiological and behavioral deficits (Abeliovich et al., 2000). Western blot analysis supports these microarray findings, showing almost complete lack of α-synuclein expression in the cerebral cortex of 1- and 3-month-old *Cln1/5* dko mice. Although immunohistological staining showed individual variability in the levels of α-synuclein protein in 1- and 3-month-old *Cln1/5* dko mice, these results support the western blot findings, showing reduced α-synuclein staining in the cortex and slightly decreased expression in the hippocampus. We suggest that the individual variability might depend on the stage of the disease, and the loss of α-synuclein expression in cortex could be linked to the early neuronal loss seen in this region in *Cln1/5* dko mice. α-synuclein might possibly have a role in NCL pathogenesis, or at least these disease mechanisms might have a significant impact on α-synuclein expression. This protein also functions as a lipid-binding protein, and lipids can regulate its oligomerization into amyloid fibrils found in Lewy bodies (Chua and Tang, 2011).

Among the most upregulated genes in *Cln1/5* dko mice were *Cap1*; complement C1q subcomponents *C1qb* and *C1qc*; and *GFAP*. *Cap1* has been implicated in a number of complex developmental and morphological processes, including endocytosis and actin polymerization (Sultana et al., 2005). Upregulation of *Cap1* was evident in all three knockout models (*Cln1* ko, *Cln5* ko and *Cln1*/*5* dko), and it is clustered on the same chromosomal region as *Ppt1* (gene mutated in *Cln1* ko), indicating a possible functional relationship between these genes (Ahtiainen et al., 2007; von Schantz et al., 2008). C1q, a key player in the classical complement pathway, is considered to be a marker for microglial activation (Färber et al., 2009) and is implicated in the pathogenesis of many neurodegenerative diseases (Nayak et al., 2010). Furthermore, it has been suggested that in the early stages of CNS neurodegenerative diseases, reactive astrocytes and C1q play a role in pathophysiological process that leads to synapse loss and neuronal death (Stevens et al., 2007). Indeed, the upregulation of *GFAP* expression is consistent with the marked astrocytosis seen

in *Cln1/5* dko brains. Our gene expression data provide further insight into the processes involved in the early stages of NCL pathogenesis. Upregulation of immune response pathways is consistent with the microglial activation we observed in the affected cerebral cortex. Decreased expression of myelin-specific genes provides evidence that defective myelination is due to a failure in myelin development processes. We suggest that NCL proteins are linked to the development of the nervous system or involved in as-yet uncharacterized neuron-specific metabolic pathways.

Conclusions

Simultaneous deletion of two NCL genes, *Cln1* and *Cln5*, has allowed us to show for the first time that early demyelination, cortical astrocytosis and microglial activation all occur prior to neuronal loss in this model. Because the loss of both *Cln1* and *Cln5* genes led to a more severe NCL phenotype in mice than the loss of only one of these genes, these results could be interpreted as further support for the existence of interactions between *Cln1* and *Cln5* gene products. Alternatively, this could simply reflect that deficiency of these genes leads to convergent pathological pathways that have a more severe combined effect. Indeed, significant accumulation of autofluorescent storage material, the ultrastructure of storage material, increased astrocytosis and microglial activation, as well as myelination defects seen in *Cln1/5* dko mice resemble the more severe pathological features of *Cln1* ko mice, whereas the onset of neuron loss is similar to that observed in *Cln5* ko mice. Decreased α-synuclein gene and protein expression in the *Cln1/5* dko brain is a new finding that might reflect the early cortical neuron loss and needs further investigation. More detailed studies are needed to obtain a comprehensive view of NCL diseases and the neurodegenerative mechanisms involved in the development of these brain disorders.

MATERIALS AND METHODS

Generation of the *Cln1/5* dko mouse model

Homozygous $Cln1^{-/-}$ (*Cln1* ko) and $Cln5^{-/-}$ (*Cln5* ko) mice (*Mus musculus*) were backcrossed to C57BL/6JRccHsd for more than ten generations, and their congeneity was confirmed with the Mouse Medium Density SNP Panel (Illumina). *Cln1* ko and *Cln5* ko mice were crossed to initially generate heterozygous and, subsequently, $Cln1^{-/-}/Cln5^{-/-}$ double-knockout (*Cln1/5* dko) offspring. These *Cln1/5* dko offspring were viable and fertile. The genotypes of the mice were determined by PCR of DNA from tail biopsies. We used systematically sampled brain or skin tissue from E16.5 to 3-month-old mice, with age- and sex-matched C57BL/6JRcc wild-type mice serving as a control strain. After sacrificing, body weight was determined.

All animal procedures were performed according to protocols approved by the ethical boards for animal experimentation of the National Public Health Institute and University of Helsinki, as well as State Provincial offices of Finland (agreement numbers ESLH 2009-05074/STH 415 A and KEK10-059). All experiments were performed in accordance with good practice of handling laboratory animals and genetically modified organisms.

Generation and characterization of murine iPS cells

Mouse embryonic fibroblasts (MEFs) from both the *Cln1/5* dko and wild-type mice (E16.5) were reprogrammed by using the retrovirus-mediated delivery of the four Yamanaka factors (Oct-3/4, Sox-2, Klf-4 and c-Myc; Addgene plasmids 13366, 13367, 13370 and 13375) (Kitamura et al., 2003) according to a published protocol (Takahashi et al., 2007). iPS cell clones were grown on leukemia inhibitory factor (LIF)-producing SNL-feeder cells (McMahon and Bradley, 1990), kindly provided by the Wellcome Trust Sanger Institute (UK), collected on the basis of colony morphology (supplementary material Fig. S1A), expanded and further purified by MACS anti-stage-specific embryonic antigen 1 (SSEA-1) MicroBeads (Miltenyi Biotech, Bergisch Gladbach, Germany). Expression of SSEA-1 (supplementary material Fig. S1A) and alkaline phosphatase (data not shown) in different clones was analyzed by ES cell characterization kit (Millipore, Billerica, MA). Expression of other ES cell marker genes (*Nanog*, *Rex-1*, *Fgf-4*, *Esg-1* and *E-ras*) in selected iPS cell clones was verified by RT-PCR (supplementary material Fig. S1B) by using primer sequences earlier described (Takahashi et al., 2007).

EB formation and analyses of EB size

To minimize the inhibitory effect of the remaining feeder cells during EB formation, all iPS cell clones were purified by MACS anti-SSEA-1 MicroBeads (Miltenyi Biotech) before starting the experiments. The number of purified cells was analyzed by Nexcelom T4 cell counter (Nexcelom Bioscience, Lawrence, MA) and 1.5×10^6 cells/clone were plated on 60-mm Petri dishes (Sterilin, Newport, UK) to facilitate EB growth in suspension in ES medium (DMEM+15% ES serum, 1× Glutamax, 0.1 mM non-essential amino acids, 0.1 mM 2-mercaptoethanol and antibiotics). Formation of EBs was followed daily by microscope. On day seven, EBs were transferred onto 12-well plates for recording images with a Leica EC3 digital camera attached to Leica DMIL microscope (Leica Microsystems, Wetzlar, Germany). The size of EBs was determined by the Las EZ program (Leica Microsystems). The average size of EBs derived from different iPS cell clones was calculated from minimum of 40 different EBs. Statistical analyses of the difference in EB size between *Cln1/5* dko and wild-type clones were assessed using the Student's *t*-test for independent samples, with unequal variances assumed. Statistical significance was considered at $P<0.05$; *P*-values are two-sided. Results are presented as means and s.e.m. EB formation was always done in pairs with *Cln1/5* dko and wild-type clones. Results were verified in three independent experiments (by using three *Cln1/5* dko and two wild-type clones).

Differentiation of iPS cells into different germ layers

To study the spontaneous differentiation potential of the produced iPS cell clones into the three primary germ layers, EBs were grown as described above for 7 days and then plated on gelatin-coated tissue culture plates. Differentiation was followed daily by microscope. The cells were fixed with 4% paraformaldehyde (PFA) and stained with goat anti-FoxA2 (1:100, Santa Cruz Biotechnology, Santa Cruz, CA), rabbit anti-β-III tubulin (1:1000, Covance, Princeton, NJ) or rabbit anti-desmin (1:500, Epitomics, Burlingame, CA) antibodies for indication of endoderm, ectoderm and mesoderm, respectively (supplementary material Fig. S2). Image processing (brightness and contrast) was performed with Adobe Photoshop and Adobe Illustrator (Adobe Systems, San Jose, CA).

Electron microscopy and autofluorescence of storage material

For electron microscopy, the brains were removed from sacrificed 3-month-old male *Cln1* ko, *Cln5* ko and *Cln1/5* dko mice and wild-type controls. Bisected brains were immersion fixed in 0.1 M phosphate buffer pH 7.4 containing 4% PFA and 2.5% glutaraldehyde for 2 hours, incubated in fresh fix solution for 2 days, and stored in 10 mM phosphate buffer at +4°C until processed further. Pieces of 1-2 mm^3 were excised from corpus callosum, thalamus, brain stem and cerebral cortex. Pieces were osmicated, dehydrated and embedded in epoxy resin. After identification of the desired anatomical regions from thin sections stained with toluidine blue, ultrathin sections were cut and contrasted with uranyl acetate and lead citrate and viewed by JEOL 1400 transmission electron microscope (JEOL, Tokyo, Japan). Images were taken with an Olympus-SIS Morada camera (Olympus, Tokyo, Japan).

For autofluorescence analysis, *Cln1* ko, *Cln5* ko, *Cln1/5* dko and wild-type mice were perfused with 4% PFA, and the brains were further immersion fixed in 4% PFA. Mouse brain sections spanning the S1BF and VPM/VPL were mounted onto gelatin-chrome-coated slides and cover-slipped with Vectashield (Vector Laboratories, Peterborough, UK). Images from each section were captured at 63× magnification using a Leica SP5 confocal microscope and a 488 nm excitation laser (Leica Microsystems). Thresholding image analysis was performed to determine the extent of endogenous autofluorescence. Three animals per group were included in the analysis. Three consecutive sections spanning the S1BF or VPM/VPL were mounted onto a chrome-gelatin-coated slide and cover-slipped. The non-overlapping images from each section were captured at 40× magnification using a Leica SP5 confocal microscope and a 488 nm excitation laser. During image capture, all parameters and calibration were kept constant. Semi-quantitative thresholding image analysis was carried out using Image Pro Plus software (Media Cybernetics, Chicago, IL) to determine the number of pixels per image that contained autofluorescent storage material.

Histological processing and Nissl staining

Brains from 3-month-old *Cln1* ko, *Cln5* ko and *Cln1/5* dko male mice and wild-type controls (n=6 per genotype) were harvested as previously described (Schmiedt et al., 2012). Briefly, the mice were perfused with 4% PFA, and the brains were removed and postfixed in 4% PFA in 0.1 M sodium phosphate buffer (pH 7.4) overnight before cryoprotection in 30% sucrose in 50 mM Tris-buffered saline (TBS) with 0.05% sodium azide, and then frozen in liquid nitrogen and stored at −80°C. The brains were bisected along the midline and cut into 40-µm frozen coronal sections (Microm freezing microtome, Thermo Fisher Scientific, Waltham, MA). A series of every sixth section through each brain was mounted onto gelatin-chrome-coated Superfrost microscope slides (VWR, Radnor, PA). Slides were air-dried overnight and incubated with 0.05% cresyl fast violet and 0.05% acetic acid (VWR) in water for 45 minute at 60°C, rinsed in distilled water and differentiated through an ascending series of alcohols, cleared in xylene and cover-slipped with DPX (VWR).

Immunohistochemistry of frozen sections

To investigate the extent of astrocytosis, microglial activation and myelination in 1- and 3-month-old male *Cln1* ko, *Cln5* ko, and *Cln1/5* dko and the wild-type control brains (n=6 per genotype), a one in six series of free-floating frozen sections were immunohistochemically stained for GFAP, cluster of differentiation (CD68) and myelin basic protein (MBP), respectively [as described previously (von Schantz et al., 2009; Schmiedt et al., 2012)]. Briefly, sections were incubated in 1% hydrogen peroxide (H_2O_2) in TBS and blocked for 40 minutes with TBS containing 0.3% Triton X-100 (TBST) and 15% normal goat serum before incubation overnight in the following polyclonal primary serums: rabbit anti-GFAP (1:4000; DAKO, Glostrup, Denmark), rat anti-CD68 (1:1000; Serotec, Oxford, UK), and rat anti-MBP (1:500; Millipore) diluted in TBS with 10% normal rabbit or rat serum and TBST. Sections were incubated for 2 hours with secondary antiserum (biotinylated goat anti-rabbit IgG (1:1000; Vector Laboratories) in TBS with 10% normal goat serum and TBST, and for 2 hours in an avidin-biotin-peroxidase complex in TBS (Vectastain ABC Elite Kit, Vector Laboratories). Immunoreactivity was visualized by 0.05% 3,3 -diaminobenzidine tetrahydrochloride (DAB) (Sigma-Aldrich, St Louis, MO) and 0.001% H_2O_2 in TBS for 10 minutes. Sections were mounted on gelatin-chrome-coated Superfrost microscope slides (WVR), and cover-slipped with DPX.

Thresholding image analysis of astrocytic and microglial phenotypes

The optical density of GFAP and CD68 immunoreactivity was assessed using semi-automated thresholding image analysis, as previously described (Bible et al., 2004; Pontikis et al., 2005). Three animals per group were included in the analysis. Briefly, 30 non-overlapping images, on triplicate sections, were taken through the thalamic VPM/VPL and cortical S1BF regions, starting from a defined anatomical landmark. Images were captured with Leica SP5 confocal microscope using a 40× objective. Image Pro Plus image analysis software (Media Cybernetics) was used to determine the area of immmunoreactivity by applying a threshold that discriminated staining from background in each image. Data were separately plotted graphically as the mean percentage area of immunoreactivity per field ± s.e.m. for each region. Differences between groups were analyzed with one-way ANOVA (more than two groups) with post-hoc Bonferroni. The level of significance was set to $P<0.05$.

Immunohistochemistry of paraffin sections

α-synuclein protein expression was analyzed from paraffin sections. Three-month-old male *Cln1* ko, *Cln5* ko, *Cln1/5* dko and wild-type control mice (n=6 per genotype) were included in the study. Brains were removed, bisected along the midline and immersion fixed with 4% PFA in PBS (pH 7.4) before embedding in paraffin. The tissue sections were cut into 5-µm sections and stained with α-synuclein antibody (rabbit polyclonal hSA-2, raised and affinity-purified at Open Biosystems, Huntsville, AL) against recombinant, full-length α-synuclein. The antibody was a kind gift from Prof. Michael G. Schlossmacher, University of Ottawa, Canada, and is described in the literature (Mollenhauer et al., 2008). Briefly, sections were deparaffinized, rehydrated in alcohol series, incubated in 5% H_2O_2 in methanol to quench endogenous peroxidase activity and rinsed with TBS. After boiling in citrate buffer (pH 6.0) for 5 minutes, the sections were blocked with 10% goat serum in TBS and incubated overnight at +4°C with primary antibody (anti-mouse α-synuclein,

1:800) in 10% goat serum in TBS. Sections were washed with TBST (0.025%) and incubated with biotinylated secondary antibody (anti-rabbit IgG, 1:200; Jackson ImmunoResearch Laboratories, Reston, VA) in 10% goat serum in TBS for one hour. Sections were treated with avidin-biotin peroxidase mix (Vectastain ABC Elite Kit, 1:400; Vector Laboratories) for 40 minutes followed by washes with TBS. Antibody binding was detected with a standard DAB reaction (Sigma-Aldrich), after which the sections were counterstained for two minutes with hematoxylin (Sigma-Aldrich). After dehydration, the sections were cleared in xylene, air-dried and cover-slipped with DPX.

Measurements of cortical thickness and regional volume

Stereological analysis was used to determine the thickness of the M1, S1BF, V1 and LEnt cortical layers, as well as cortical and hippocampal volumes. We used *StereoInvestigator* software (Microbrightfield, Williston, VT) to obtain unbiased Cavalieri estimates from 40-µm Nissl-stained cryosections from *Cln1* ko, *Cln5* ko, *Cln1/5* dko and wild-type male mice (n=6 per genotype) at 3 months of age, with no prior knowledge of genotype. The boundaries of brain regions were defined by reference to landmarks described by Paxinos and Franklin (Paxinos and Franklin, 2001). All analyses were carried out on a Zeiss, Axioskop 2 MOT microscope (Carl Zeiss, Welwyn Garden City, UK) linked to a DAGE-MTI CCD-100 camera (DAGE-MTI, Michigan City, IN). Measurements of the thickness of M1, S1BF, V1 and LEnt were made in three consecutive Nissl-stained sections with ten measurements made from the white matter to the pial surface of the cortex within each section (Bible et al., 2004). Results were expressed as the mean cortical thickness (micrometers per region). Regional volumes of cortex and hippocampus were determined by placing an appropriately spaced sampling grid over sections and the number of points covering the relevant areas was assessed using a 2.5× objective. Results are expressed in cubic micrometers and the mean volume of each region was calculated for each genotype. The mean coefficient of error (CE) for all individual Cavalieri estimates was calculated according to the method of Gundersen and Jensen (Gundersen and Jensen, 1987) and was ≤0.1 in all these analyses. Differences between groups were analyzed with one-way ANOVA with post-hoc Bonferroni (GraphPad Software, La Jolla, CA). The level of significance was set to P<0.05.

Counts of neuronal number

The design-based optical fractionator probe was used to estimate cell number in Nissl-stained sections in cortical S1BF and VPM/VPL. Nissl-stained cells were only counted if they had a neuronal morphology and a clearly identifiable nucleolus. A line was traced around the boundary of the region of interest, a grid was superimposed and cells were counted using a 100× objective within a series of dissector frames placed according to intersections of the sampling grid. Different grid and dissector sizes were determined according to each brain region using a CE value ≤0.1 to indicate sampling efficiency. Layer V of the S1BF grid was 175×175 µm, frame 70×40 µm; layer VI grid was 200×175 µm, frame 55×40 µm; and layer IV grid was 150×150 µm, frame 70×40 µm. For VPM/VPL, the grid was 175×175 µm, frame 70×40 µm. A series of every sixth Nissl-stained sections was used for all the brain regions. Differences between groups were analyzed with one-way ANOVA (more than two groups) with post-hoc Bonferroni. The level of significance was set to P<0.05.

Plasma lipid analysis

Female 1-month-old *Cln5* ko, *Cln1* ko and *Cln1/5* dko mice (n=8 per genotype) and wild-type controls were fasted for a 4-hour period and blood taken for plasma lipid and lipoprotein analysis. Iodoacetic acid (1 mM final) was immediately added to samples to avoid lecithin-cholesterol acyltransferase (LCAT) activity. Triglycerides and total cholesterol were measured using enzymatic methods (GPO-PAP 1488872 kit and CHOD-PAP 1489232 kit, respectively; Roche Diagnostics, Basel, Switzerland). Mouse apoA-1 was quantified by sandwich ELISA (van Haperen et al., 2000) and PLTP activity measured using radiometric assay (Jauhiainen and Ehnholm, 2005). For the analysis of cholesterol distribution in lipoproteins, plasma samples were pooled and fractionated by fast-performance liquid chromatography (FPLC) using high-resolution Superose 6 size-exclusion chromatography columns (GE Healthcare, Waukesha, WI) to separate the lipoprotein classes. Two pools per genotype (wild-type, *Cln5* ko, *Cln1* ko and *Cln1/5* dko) were analyzed (three independent plasma samples per genotype). P-values were evaluated using one-way ANOVA, with P<0.05 considered as statistically significant.

Gene expression profiling

Comparative gene expression profiling was performed from the 1-month-old *Cln1/5* dko male mice and wild-type controls (n=6 per genotype). Cortices from the left hemisphere of wild-type controls and *Cln1/5* dko mice were excised and the RNA isolated with Qiagen RNA Lipid Tissue Kit (Qiagen, Hilden, Germany). Purity of RNA was verified with Agilent 2100 Bioanalyzer (Agilent Technologies, Santa Clara, CA) and its concentration was determined with NanoDrop (Thermo Fisher Scientific). Total RNA in a 400 ng sample was labeled and fragmented. Hybridization, post-hybridization washes, staining and scanning were performed according to the manufacturer's instructions (Applied Biosystems, Foster City, CA). Gene expression profiles were determined using the Illumina MouseWG-6 v2.0 Expression BeadChip and GenomeStudio Data Analysis Software (Illumina, San Diego, CA). Gene expression analysis was performed with Chipster v1.4.7 analysis software (CSC, Espoo, Finland), and data normalization was carried out using the quantile method. Quality control was performed to ensure the technical quality of the samples. P-values (adjusted with conditional testing) were used to determine the significantly up- and downregulated genes (P<0.05). Pathway analysis from the up- or downregulated genes (according to Student's t-test, P<0.05) was performed with DAVID Bioinformatics Resources 6.7 software (Huang et al., 2009a; Huang et al., 2009b), and the Benjamini-Hochberg method was used for multiple hypothesis testing correction of the P-values.

Quantitative real-time RT-PCR

Quantitative real-time RT-PCR was performed as described previously (Schmiedt et al., 2012). Briefly, RNA from frozen cortices of 1-month-old *Cln1/5* dko (n=6) and wild-type control (n=6) mice was isolated as described in the previous paragraph. RNA was treated with DNase I (Qiagen) in order to eliminate genomic DNA. The reverse transcription reactions were carried out on 10 ng of

RNA using TaqMan Reverse Transcription Reagents with random hexamer primers (Applied Biosystems, Foster City, CA). To average out the inter-individual variability, three different reverse transcription reactions were performed for each sample. TaqMan Gene Expression Array of selected genes was purchased from Applied Biosystems (Snca: Mm01188700_m1). The mRNA expression levels of this gene and a standard house-keeping gene, mouse TATA-box binding protein (Tbp: Mm00446970_m1), were quantified with ABI Prism 7000 sequence detection system (Applied Biosystems). The PCR reactions (10 µl) were carried out with TaqMan Universal Master Mix according to manufacturer's instructions using the following parameters: 50°C for 2 minutes, 95°C for 10 minutes, 40 cycles of 95°C for 15 seconds and 60°C for 1 minutes. Relative levels of the selected genes were calculated using the $\Delta\Delta C_T$ method, as described previously (Kopra et al., 2004). The absolute change in expression level is given by $2^{-\Delta\Delta CT}$.

Western blotting

Whole brains without cerebellum (denoted as 'cerebrum') and cortices of 1- and 3-month-old *Cln1* ko (*n*=3), *Cln5* ko (*n*=3), *Cln1/5 dko* (*n*=5) and wild-type control (*n*=4) mice were homogenized in extraction buffer (50 mM HEPES, pH 7.4, 100 mM NaCl, 5 mM $MgCl_2$, 0.5% Triton X-100) supplemented with Protease Inhibitor Cocktail (Sigma-Aldrich) using Precellys CK14 lysing tubes (Bertin Technologies, France). The homogenates were clarified by centrifugation at 1000 ***g*** for 10 minutes in a Beckman TLA 100.3 rotor at +4°C. Total protein concentrations were estimated by DC Protein Assay (Bio-Rad, Hercules, CA) and equal amounts of total protein (30 µg) were analyzed by western blotting. Protein samples were boiled and run on a 14% SDS-PAGE gel. After the transfer to nitrocellulose membrane (Hybond ECL, GE Healthcare), the blot was blocked in 5% milk powder in TBST and incubated with primary antibody (mouse-anti-α-synuclein, 1:1000; Cell Signaling, Danvers, MA) followed by the incubation with HRP-conjugated goat-anti-mouse secondary antiserum (1:5000; DAKO). Immunoreactivity was visualized by enhanced chemiluminescence assay (Western Lightning-ECL, PerkinElmer, Waltham, MA). β-III tubulin (1:1000; Millipore) expression was used as a loading control. Densitometric analysis of the autoradiograms was performed using NIH ImageJ 1.41o software. Student's *t*-test was used for the statistical analyses. Three animals per group were included in the analysis.

ACKNOWLEDGEMENTS

Essi Kaiharju is thanked for the excellent technical assistance with mouse experiments; Jari Metso and Sari Nuutinen are thanked for the plasma lipid and PLTP analyses; and Seija Puomilahti and Anne Nyberg are thanked for the help with the cell culturing and iPS cell analyses. We also thank Katriina Aalto-Setälä for helping to establish the iPS technology in the lab, and Outi Kopra for the critical comments on the manuscript.

COMPETING INTERESTS

The authors declare that they do not have any competing or financial interests.

AUTHOR CONTRIBUTIONS

All authors were involved in drafting the article, and all authors approved the final version to be published. T.B., A.K., A.J. and J.D.C. conceived and designed the experiments. T.B., M.-L.S., A.M.W. and A.K. performed the experiments. J.T. analyzed the electron microscopy data, M.J. analyzed the lipid metabolism data, and T.B. and J.S. analyzed the microarray data. T.B., J.D.C., A.K. and A.J. wrote the manuscript.

FUNDING

This work was financially supported by the Academy of Finland, Centre of Excellence in Complex Disease Genetics [A.J., A.K., M.-L.S., grant number 213506], the Academy of Finland [T.B., grant number 139319], the Sigrid Juselius Foundation [A.J., A.K., M.-L.S., T.B.], the Batten Disease Support and Research Association [J.D.C.], the Batten Disease Family Association [J.D.C.], the Bletsoe Family [J.D.C., A.M.W.] and the Natalie Fund [J.D.C.].

SUPPLEMENTARY MATERIAL

Supplementary material for this article is available at http://dmm.biologists.org/lookup/suppl/doi:10.1242/dmm.010140/-/DC1

REFERENCES

Abeliovich, A., Schmitz, Y., Fariñas, I., Choi-Lundberg, D., Ho, W. H., Castillo, P. E., Shinsky, N., Verdugo, J. M., Armanini, M., Ryan, A. et al. (2000). Mice lacking alpha-synuclein display functional deficits in the nigrostriatal dopamine system. *Neuron* **25**, 239-252.

Ahtiainen, L., Kolikova, J., Mutka, A. L., Luiro, K., Gentile, M., Ikonen, E., Khiroug, L., Jalanko, A. and Kopra, O. (2007). Palmitoyl protein thioesterase 1 (Ppt1)-deficient mouse neurons show alterations in cholesterol metabolism and calcium homeostasis prior to synaptic dysfunction. *Neurobiol. Dis.* **28**, 52-64.

Bible, E., Gupta, P., Hofmann, S. L. and Cooper, J. D. (2004). Regional and cellular neuropathology in the palmitoyl protein thioesterase-1 null mutant mouse model of infantile neuronal ceroid lipofuscinosis. *Neurobiol. Dis.* **16**, 346-359.

Camp, L. A. and Hofmann, S. L. (1993). Purification and properties of a palmitoyl-protein thioesterase that cleaves palmitate from H-Ras. *J. Biol. Chem.* **268**, 22566-22574.

Chrast, R., Saher, G., Nave, K. A. and Verheijen, M. H. (2011). Lipid metabolism in myelinating glial cells: lessons from human inherited disorders and mouse models. *J. Lipid Res.* **52**, 419-434.

Chua, C. E. and Tang, B. L. (2011). Rabs, SNAREs and α-synuclein—membrane trafficking defects in synucleinopathies. *Brain Res. Rev.* **67**, 268-281.

Colhoun, H. M., Scheek, L. M., Rubens, M. B., Van Gent, T., Underwood, S. R., Fuller, J. H. and Van Tol, A. (2001). Lipid transfer protein activities in type 1 diabetic patients without renal failure and nondiabetic control subjects and their association with coronary artery calcification. *Diabetes* **50**, 652-659.

Cooper, J. D. (2010). The neuronal ceroid lipofuscinoses: the same, but different? *Biochem. Soc. Trans.* **38**, 1448-1452.

Cooper, J. D., Russell, C. and Mitchison, H. M. (2006). Progress towards understanding disease mechanisms in small vertebrate models of neuronal ceroid lipofuscinosis. *Biochim. Biophys. Acta* **1762**, 873-889.

Cullen, V., Lindfors, M., Ng, J., Paetau, A., Swinton, E., Kolodziej, P., Boston, H., Saftig, P., Woulfe, J., Feany, M. B. et al. (2009). Cathepsin D expression level affects alpha-synuclein processing, aggregation, and toxicity in vivo. *Mol. Brain* **2**, 5.

Elshatory, Y., Brooks, A. I., Chattopadhyay, S., Curran, T. M., Gupta, P., Ramalingam, V., Hofmann, S. L. and Pearce, D. A. (2003). Early changes in gene expression in two models of Batten disease. *FEBS Lett.* **538**, 207-212.

Färber, K., Cheung, G., Mitchell, D., Wallis, R., Weihe, E., Schwaeble, W. and Kettenmann, H. (2009). C1q, the recognition subcomponent of the classical pathway of complement, drives microglial activation. *J. Neurosci. Res.* **87**, 644-652.

Gehrmann, J., Matsumoto, Y. and Kreutzberg, G. W. (1995). Microglia: intrinsic immuneffector cell of the brain. *Brain Res. Brain Res. Rev.* **20**, 269-287.

Gundersen, H. J. and Jensen, E. B. (1987). The efficiency of systematic sampling in stereology and its prediction. *J. Microsc.* **147**, 229-263.

Haltia, M. (2003). The neuronal ceroid-lipofuscinoses. *J. Neuropathol. Exp. Neurol.* **62**, 1-13.

Haltia, M. (2006). The neuronal ceroid-lipofuscinoses: from past to present. *Biochim. Biophys. Acta* **1762**, 850-856.

Hellsten, E., Vesa, J., Heiskanen, M., Mäkelä, T. P., Järvelä, I., Cowell, J. K., Mead, S., Alitalo, K., Palotie, A. and Peltonen, L. (1995). Identification of YAC clones for human chromosome 1p32 and physical mapping of the infantile neuronal ceroid lipofuscinosis (INCL) locus. *Genomics* **25**, 404-412.

Holmberg, V., Jalanko, A., Isosomppi, J., Fabritius, A. L., Peltonen, L. and Kopra, O. (2004). The mouse ortholog of the neuronal ceroid lipofuscinosis CLN5 gene encodes a soluble lysosomal glycoprotein expressed in the developing brain. *Neurobiol. Dis.* **16**, 29-40.

Holness, C. L., da Silva, R. P., Fawcett, J., Gordon, S. and Simmons, D. L. (1993). Macrosialin, a mouse macrophage-restricted glycoprotein, is a member of the lamp/lgp family. *J. Biol. Chem.* **268**, 9661-9666.

Huang, W., Sherman, B. T. and Lempicki, R. A. (2009a). Systematic and integrative analysis of large gene lists using DAVID bioinformatics resources. *Nat. Protoc.* **4**, 44-57.

Huang, W., Sherman, B. T. and Lempicki, R. A. (2009b). Bioinformatics enrichment tools: paths toward the comprehensive functional analysis of large gene lists. *Nucleic Acids Res.* **37**, 1-13.

Jalanko, A. and Braulke, T. (2009). Neuronal ceroid lipofuscinoses. *Biochim. Biophys. Acta* **1793**, 697-709.

Jalanko, A., Vesa, J., Manninen, T., von Schantz, C., Minye, H., Fabritius, A. L., Salonen, T., Rapola, J., Gentile, M., Kopra, O. et al. (2005). Mice with Ppt1Deltaex4 mutation replicate the INCL phenotype and show an inflammation-associated loss of interneurons. *Neurobiol. Dis.* **18**, 226-241.

Jauhiainen, M. and Ehnholm, C. (2005). Determination of human plasma phospholipid transfer protein mass and activity. *Methods* **36**, 97-101.

Kielar, C., Maddox, L., Bible, E., Pontikis, C. C., Macauley, S. L., Griffey, M. A., Wong, M., Sands, M. S. and Cooper, J. D. (2007). Successive neuron loss in the thalamus and cortex in a mouse model of infantile neuronal ceroid lipofuscinosis. *Neurobiol. Dis.* **25**, 150-162.

Kitamura, T., Koshino, Y., Shibata, F., Oki, T., Nakajima, H., Nosaka, T. and Kumagai, H. (2003). Retrovirus-mediated gene transfer and expression cloning: powerful tools in functional genomics. *Exp. Hematol.* **31**, 1007-1014.

Kopra, O., Vesa, J., von Schantz, C., Manninen, T., Minye, H., Fabritius, A. L., Rapola, J., van Diggelen, O. P., Saarela, J., Jalanko, A. et al. (2004). A mouse model for Finnish variant late infantile neuronal ceroid lipofuscinosis, CLN5, reveals neuropathology associated with early aging. *Hum. Mol. Genet.* **13**, 2893-2906.

Kousi, M. (2012). *Dissection of the Genetic Background of Childhood Onset Progressive Myoclonic Epilepsies*. PhD thesis, 130 pp., University of Helsinki and Neuroscience Center and Folkhälsan Institute of Genetics, Helsinki, Finland.

Kousi, M., Lehesjoki, A. E. and Mole, S. E. (2012). Update of the mutation spectrum and clinical correlations of over 360 mutations in eight genes that underlie the neuronal ceroid lipofuscinoses. *Hum. Mutat.* **33**, 42-63.

Kuronen, M., Lehesjoki, A. E., Jalanko, A., Cooper, J. D. and Kopra, O. (2012). Selective spatiotemporal patterns of glial activation and neuron loss in the sensory thalamocortical pathways of neuronal ceroid lipofuscinosis 8 mice. *Neurobiol. Dis.* **47**, 444-457.

Lyly, A., Marjavaara, S. K., Kyttälä, A., Uusi-Rauva, K., Luiro, K., Kopra, O., Martinez, L. O., Tanhuanpää, K., Kalkkinen, N., Suomalainen, A. et al. (2008). Deficiency of the INCL protein Ppt1 results in changes in ectopic F1-ATP synthase and altered cholesterol metabolism. *Hum. Mol. Genet.* **17**, 1406-1417.

Lyly, A., von Schantz, C., Heine, C., Schmiedt, M.-L., Sipilä, T., Jalanko, A. and Kyttälä, A. (2009). Novel interactions of CLN5 support molecular networking between Neuronal Ceroid Lipofuscinosis proteins. *BMC Cell Biol.* **10**, 83.

Macauley, S. L., Pekny, M. and Sands, M. S. (2011). The role of attenuated astrocyte activation in infantile neuronal ceroid lipofuscinosis. *J. Neurosci.* **31**, 15575-15585.

Mamo, A., Jules, F., Dumaresq-Doiron, K., Costantino, S. and Lefrancois, S. (2012). The role of ceroid lipofuscinosis neuronal protein 5 (CLN5) in endosomal sorting. *Mol. Cell. Biol.* **32**, 1855-1866.

McMahon, A. P. and Bradley, A. (1990). The Wnt-1 (int-1) proto-oncogene is required for development of a large region of the mouse brain. *Cell* **62**, 1073-1085.

Meng, X. L., Shen, J. S., Kawagoe, S., Ohashi, T., Brady, R. O. and Eto, Y. (2010). Induced pluripotent stem cells derived from mouse models of lysosomal storage disorders. *Proc. Natl. Acad. Sci. USA* **107**, 7886-7891.

Mole, S. E., Williams, R. E. and Goebel, H. H. (eds) (2011). *The Neuronal Ceroid Lipofuscinoses (Batten Disease)*. Oxford, UK: Oxford University Press.

Mollenhauer, B., Cullen, V., Kahn, I., Krastins, B., Outeiro, T. F., Pepivani, I., Ng, J., Schulz-Schaeffer, W., Kretzschmar, H. A., McLean, P. J. et al. (2008). Direct quantification of CSF alpha-synuclein by ELISA and first cross-sectional study in patients with neurodegeneration. *Exp. Neurol.* **213**, 315-325.

Nayak, A., Ferluga, J., Tsolaki, A. G. and Kishore, U. (2010). The non-classical functions of the classical complement pathway recognition subcomponent C1q. *Immunol. Lett.* **131**, 139-150.

Partanen, S., Haapanen, A., Kielar, C., Pontikis, C., Alexander, N., Inkinen, T., Saftig, P., Gillingwater, T. H., Cooper, J. D. and Tyynelä, J. (2008). Synaptic changes in the thalamocortical system of cathepsin D-deficient mice: a model of human congenital neuronal ceroid-lipofuscinosis. *J. Neuropathol. Exp. Neurol.* **67**, 16-29.

Paxinos, G. and Franklin, K. B. J. (2001). *The Mouse Brain in Stereotaxic Coordinates*, 2nd edn. San Diego, CA: Academic Press.

Perry, V. H., Nicoll, J. A. and Holmes, C. (2010). Microglia in neurodegenerative disease. *Nat. Rev. Neurol.* **6**, 193-201.

Pontikis, C. C., Cotman, S. L., MacDonald, M. E. and Cooper, J. D. (2005). Thalamocortical neuron loss and localized astrocytosis in the Cln3Deltaex7/8 knock-in mouse model of Batten disease. *Neurobiol. Dis.* **20**, 823-836.

Ruipérez, V., Darios, F. and Davletov, B. (2010). Alpha-synuclein, lipids and Parkinson's disease. *Prog. Lipid Res.* **49**, 420-428.

Santavuori, P. (1988). Neuronal ceroid-lipofuscinoses in childhood. *Brain Dev.* **10**, 80-83.

Savukoski, M., Klockars, T., Holmberg, V., Santavuori, P., Lander, E. S. and Peltonen, L. (1998). CLN5, a novel gene encoding a putative transmembrane protein mutated in Finnish variant late infantile neuronal ceroid lipofuscinosis. *Nat. Genet.* **19**, 286-288.

Schmiedt, M.-L., Bessa, C., Heine, C., Ribeiro, M. G., Jalanko, A. and Kyttälä, A. (2010). The neuronal ceroid lipofuscinosis protein CLN5: new insights into cellular maturation, transport, and consequences of mutations. *Hum. Mutat.* **31**, 356-365.

Schmiedt, M.-L., Blom, T., Blom, T., Kopra, O., Wong, A., von Schantz-Fant, C., Ikonen, E., Kuronen, M., Jauhiainen, M., Cooper, J. D. et al. (2012). Cln5-deficiency in mice leads to microglial activation, defective myelination and changes in lipid metabolism. *Neurobiol. Dis.* **46**, 19-29.

Siggins, S., Rye, K.-A., Olkkonen, V. M., Jauhiainen, M. and Ehnholm, C. (2007). Human plasma phospholipid transfer protein (PLTP) – structural and functional features. In *High-Density Lipoproteins* (ed. C. J. Fielding), pp. 183-205. Weinheim, Germany: Wiley-VCH Verlag.

Stevens, B., Allen, N. J., Vazquez, L. E., Howell, G. R., Christopherson, K. S., Nouri, N., Micheva, K. D., Mehalow, A. K., Huberman, A. D., Stafford, B. et al. (2007). The classical complement cascade mediates CNS synapse elimination. *Cell* **131**, 1164-1178.

Sultana, H., Rivero, F., Blau-Wasser, R., Schwager, S., Balbo, A., Bozzaro, S., Schleicher, M. and Noegel, A. A. (2005). Cyclase-associated protein is essential for the functioning of the endo-lysosomal system and provides a link to the actin cytoskeleton. *Traffic* **6**, 930-946.

Takahashi, K., Okita, K., Nakagawa, M. and Yamanaka, S. (2007). Induction of pluripotent stem cells from fibroblast cultures. *Nat. Protoc.* **2**, 3081-3089.

Tyynelä, J., Palmer, D. N., Baumann, M. and Haltia, M. (1993). Storage of saposins A and D in infantile neuronal ceroid-lipofuscinosis. *FEBS Lett.* **330**, 8-12.

Tyynelä, J., Cooper, J. D., Khan, M. N., Shemilts, S. J. and Haltia, M. (2004). Hippocampal pathology in the human neuronal ceroid-lipofuscinoses: distinct patterns of storage deposition, neurodegeneration and glial activation. *Brain Pathol.* **14**, 349-357.

Uversky, V. N. (2008). Alpha-synuclein misfolding and neurodegenerative diseases. *Curr. Protein Pept. Sci.* **9**, 507-540.

van Haperen, R., van Tol, A., Vermeulen, P., Jauhiainen, M., van Gent, T., van den Berg, P., Ehnholm, S., Grosveld, F., van der Kamp, A. and de Crom, R. (2000). Human plasma phospholipid transfer protein increases the antiatherogenic potential of high density lipoproteins in transgenic mice. *Arterioscler. Thromb. Vasc. Biol.* **20**, 1082-1088.

Vekrellis, K., Xilouri, M., Emmanouilidou, E., Rideout, H. J. and Stefanis, L. (2011). Pathological roles of α-synuclein in neurological disorders. *Lancet Neurol.* **10**, 1015-1025.

Vesa, J., Hellsten, E., Verkruyse, L. A., Camp, L. A., Rapola, J., Santavuori, P., Hofmann, S. L. and Peltonen, L. (1995). Mutations in the palmitoyl protein thioesterase gene causing infantile neuronal ceroid lipofuscinosis. *Nature* **376**, 584-587.

Vesa, J., Chin, M. H., Oelgeschläger, K., Isosomppi, J., DellAngelica, E. C., Jalanko, A. and Peltonen, L. (2002). Neuronal ceroid lipofuscinoses are connected at molecular level: interaction of CLN5 protein with CLN2 and CLN3. *Mol. Biol. Cell* **13**, 2410-2420.

von Schantz, C., Saharinen, J., Kopra, O., Cooper, J. D., Gentile, M., Hovatta, I., Peltonen, L. and Jalanko, A. (2008). Brain gene expression profiles of Cln1 and Cln5 deficient mice unravels common molecular pathways underlying neuronal degeneration in NCL diseases. *BMC Genomics* **9**, 146.

von Schantz, C., Kielar, C., Hansen, S. N., Pontikis, C. C., Alexander, N. A., Kopra, O., Jalanko, A. and Cooper, J. D. (2009). Progressive thalamocortical neuron loss in Cln5 deficient mice: Distinct effects in Finnish variant late infantile NCL. *Neurobiol. Dis.* **34**, 308-319.

Weimer, J. M., Custer, A. W., Benedict, J. W., Alexander, N. A., Kingsley, E., Federoff, H. J., Cooper, J. D. and Pearce, D. A. (2006). Visual deficits in a mouse model of Batten disease are the result of optic nerve degeneration and loss of dorsal lateral geniculate thalamic neurons. *Neurobiol. Dis.* **22**, 284-293.